The Astrophysical Journal, 1006:205 (23pp), 2026 August 1 https://doi.org/10.3847/1538-4357/ae80cd

Beyond the Dot: An LRD-like Nucleus at the Heart of an IR-bright Galaxy and its Implications for High-redshift LRDs

Pierluigi Rinaldi[1], George H. Rieke[1], Zihao Wu[2], Carys J. E. Gilbert[3], Fabio Pacucci[2,4], Luigi Barchiesi[3,5,6], Stacey Alberts[1,7], Stefano Carniani[8], Andrew J. Bunker[9], Rachana Bhatawdekar[10], Francesco D'Eugenio[11,12], Zhiyuan Ji[1], Benjamin D. Johnson[2], Kevin Hainline[1], Vasily Kokorev[13], Nimisha Kumari[7], Edoardo Iani[14], Jianwei Lyu[1], Roberto Maiolino[11,12,15], Eleonora Parlanti[8], Brant E. Robertson[16], Yang Sun[1], Cristian Vignali[17,18], Christina C. Williams[19], Christopher N. A. Willmer[1], and Yongda Zhu[1]

[1] Steward Observatory, University of Arizona, 933 North Cherry Avenue, Tucson, AZ 85721, USA; prinaldi@arizona.edu
[2] Center for Astrophysics|Harvard & Smithsonian, 60 Garden St., Cambridge MA 02138, USA
[3] Department of Astronomy, University of Cape Town, Private Bag X3, Rondebosch 7701, South Africa
[4] Black Hole Initiative, Harvard University, 20 Garden St, Cambridge, MA 02138, USA
[5] Inter-University Institute for Data Intensive Astronomy, University of Cape Town, Private Bag X3, Rondebosch 7701, South Africa
[6] INAF–Istituto di Radioastronomia, Via Piero Gobetti 101, I-40129 Bologna, Italy
[7] AURA for the European Space Agency (ESA), Space Telescope Science Institute, 3700 San Martin Dr., Baltimore, MD 21218, USA
[8] Scuola Normale Superiore, Piazza dei Cavalieri 7, I-56126 Pisa, Italy
[9] Department of Physics, University of Oxford, Denys Wilkinson Building, Keble Road, Oxford OX1 3RH, UK
[10] European Space Agency (ESA), European Space Astronomy Centre (ESAC), Camino Bajo del Castillo s/n, 28692, Villanueva de la Cañada, Madrid, Spain
[11] Kavli Institute for Cosmology, University of Cambridge, Madingley Road, Cambridge, CB3 0HA, UK
[12] Cavendish Laboratory, University of Cambridge, 19 JJ Thomson Avenue, Cambridge, CB3 0HE, UK
[13] Department of Astronomy, The University of Texas at Austin, Austin, TX 78712, USA
[14] Institute of Science and Technology Austria (ISTA), Am Campus 1, 3400 Klosterneuburg, Austria
[15] Department of Physics and Astronomy, University College London, Gower Street, London WC1E 6BT, UK
[16] Department of Astronomy and Astrophysics, University of California, Santa Cruz, 1156 High Street, Santa Cruz, CA 95064, USA
[17] Dipartimento di Fisica e Astronomia, Alma Mater Studiorum, Università degli Studi di Bologna, Via Gobetti 93/2, 40129 Bologna, Italy
[18] INAF–Osservatorio di Astrofisica e Scienza dello Spazio di Bologna, Via Gobetti 93/3, 40129 Bologna, Italy
[19] NSF National Optical-Infrared Astronomy Research Laboratory, 950 North Cherry Avenue, Tucson, AZ 85719, USA
Received 2025 July 24; revised 2026 June 14; accepted 2026 June 16; published 2026 July 29

Abstract

Little red dots (LRDs) are compact, red sources discovered by JWST at high redshift ($z \gtrsim 4$), marked by distinctive "V-shaped" spectral energy distributions (SEDs) and often interpreted as rapidly accreting active galactic nuclei (AGNs). Their true nature remains unclear though, and their evolutionary connection to their lower-redshift counterparts is still poorly constrained. Thus, we present WISEA J123635.56+621424.2 (here dubbed the Saguaro), a $z = 2.0145$ galaxy in GOODS-North, as a possible analog of high-redshift LRDs and a potential missing link in their evolutionary path toward lower-redshift systems. It features a compact LRD-like nucleus surrounded by a face-on spiral host. Its connections to LRDs include the following: (1) its nuclear spectrum shows a clear "V-shaped" SED, and (2) when redshifted to $z = 7$, surface brightness dimming makes the host undetectable, thus mimicking an LRD. This suggests that high-redshift LRDs may be embedded in extended hosts. To test this, we stack rest-frame UV images of 99 photometrically selected LRDs, revealing faint, diffuse emission. Stacking in redshift bins reveals mild radial growth, consistent with the expected galaxy size evolution. A simple analytic model confirms that surface brightness dimming alone can explain their compact appearance. Lastly, we show that the Saguaro is not unique by describing similar objects from the literature at $z \lesssim 3.5$. Taken together, our results support a scenario in which LRDs may not be a distinct population, but could be the visible nuclei of galaxies undergoing a short-lived, (perhaps) AGN-dominated evolutionary phase, with their compact, red appearance driven largely by observational biases.

Unified Astronomy Thesaurus concepts: AGN host galaxies (2017); Active galactic nuclei (16); Infrared astronomy (786); Star formation (1569); Galaxy evolution (594); Near infrared astronomy (1093); Galaxy formation (595); Spectral energy distribution (2129); Galaxies (573); X-ray astronomy (1810); X-ray active galactic nuclei (2035)

1. Introduction

One of the goals of building JWST (J. P. Gardner et al. 2023) was to see far enough back in time that fundamental differences would be apparent in galaxies and active galactic nuclei (AGNs). Pre-JWST, although number counts of nearly all classes of objects were found to evolve strongly, the properties of individual objects seemed familiar in comparison with relatively nearby analogs (e.g., for quasars, see X. Fan et al. 2023, and for lower luminosities, see P. Padovani 2017). This implied that we were not yet reaching far enough back to witness their birth and earliest stages of evolution.

JWST has now extended our view well into the infrared, providing the sensitivity and wavelength coverage needed to study AGN populations deep into the early Universe.

For example, Seyfert-luminosity AGNs at $z > 4$ appear to host significantly overmassive supermassive black holes (SMBHs; e.g., Y. Harikane et al. 2023; R. Maiolino et al. 2024; F. Pacucci et al. 2023). Even more interestingly, JWST has unveiled an apparently new class of compact, red sources, commonly referred to as "little red dots" (LRDs; e.g., L. J. Furtak et al. 2023; M. Killi et al. 2024; V. Kokorev et al. 2023, 2024; H. Übler et al. 2023; H. B. Akins et al. 2025; G. Barro et al. 2024a; J. E. Greene et al. 2024; K. N. Hainline et al. 2025; D. D. Kocevski et al. 2025; J. Matthee et al. 2024; P. G. Pérez-González et al. 2024; C. C. Williams et al. 2024; P. Rinaldi et al. 2025a, 2026).

These sources have attracted significant attention because of their puzzling properties. For instance, they are compact and red at rest-frame optical wavelengths, yet blue in the UV, where they often display complex morphologies that may indicate merger activity (P. Rinaldi et al. 2025a). They show the characteristic "V-shaped" spectral energy distribution (SED), with a turnover typically occurring around the Balmer limit (D. J. Setton et al. 2025). These sources defy classical templates of star-forming galaxies and AGNs (see discussion in, e.g., A. de Graaff et al. 2025a; X. Ji et al. 2025). They also show broad permitted emission lines, typically interpreted as evidence for AGN activity (e.g., R. Maiolino et al. 2024; F. Pacucci et al. 2023). Under this interpretation, many studies suggest that LRDs host overmassive black holes relative to their galaxies ($M_\bullet \approx 10^{6-8}\, M_\odot$; e.g., L. J. Furtak et al. 2023; M. Killi et al. 2024; V. Kokorev et al. 2023; F. Pacucci et al. 2023; J. Matthee et al. 2024; P. Rinaldi et al. 2025a; J. Zhang et al. 2026), challenging models of early black hole growth. However, their role and relative importance in AGN evolution remain uncertain, especially because their luminosities and black hole mass estimates are still highly uncertain.

An alternative interpretation is the recently proposed "black hole star" (BH*) scenario (e.g., D. Kido et al. 2025; H. Liu et al. 2025; R. P. Naidu et al. 2025), in which LRDs are powered by an unknown central engine embedded in a dense, partly ionized, high-column-density gas layer ($n_H \approx 10^{8-10}$, cm^{-3}; $N_H \approx 10^{23-24}$, cm^{-2}). This configuration may explain the strong Balmer breaks, Balmer absorption, and intense Balmer emission observed in some LRDs (e.g., A. de Graaff et al. 2025a, 2025b; X. Ji et al. 2025; R. P. Naidu et al. 2025). In this framework, broad Balmer lines can arise from exponential profiles produced by electron scattering and radiative-transfer effects, reducing the inferred black hole masses and easing the tension with local black hole–stellar mass relations (e.g., R. P. Naidu et al. 2025; V. Rusakov et al. 2026). However, no coherent picture has yet emerged, and the nature of LRDs remains unclear.

Furthermore, they are typically X-ray and radio faint (T. T. Ananna et al. 2024; G. Mazzolari et al. 2026; M. Yue et al. 2024; R. Maiolino et al. 2025; K. Perger et al. 2025), although a few X-ray detections have been reported (D. D. Kocevski et al. 2025; R. E. Hviding et al. 2026) and some radio-detected cases also exist (Y. Zhong et al. 2026). Their infrared properties are equally puzzling: while some studies report warm/hot dust signatures (e.g., G. Barro et al. 2026b), others find a deficit at these wavelengths (e.g., C. C. Williams et al. 2024). However, MIRI-based stacking analyses suggest that, on average, LRDs do show warm/hot dust emission (e.g., I. Delvecchio et al. 2025).

Finally, LRDs appear abundant at $z > 4$ (≈100 times more numerous than quasars at similar M_{UV} and redshift; V. Kokorev et al. 2024; H. B. Akins et al. 2025; D. D. Kocevski et al. 2025; P. Rinaldi et al. 2026), yet decline rapidly at $z < 4$ (e.g., Bisigello (Euclid) et al. 2025; Y. Ma et al. 2026). However, recent studies have suggested that selection biases may play an important role in shaping the inferred demographics of LRDs across cosmic time (e.g., P. Rinaldi et al. 2026). Together with the diverse properties observed in these sources, this suggests that LRDs may represent a far more heterogeneous population than initially thought. Despite the large number of studies published since their discovery, their true nature remains debated, requiring a multifaceted approach to characterize them. Given their likely heterogeneous nature and the uncertainty surrounding their physical origin, throughout this work we refer to LRDs as photometrically selected compact, red sources with a "V-shaped" SED.

In this work, we want to address two fundamental questions: *what do these sources evolve into as the Universe matures?* and *do they emerge from ordinary galaxies, or are they born in fundamentally different environments?* Answering the first question is difficult as observations have shown that the number density of LRDs drops dramatically toward lower redshifts (D. D. Kocevski et al. 2025; V. Kokorev et al. 2024; Y. Ma et al. 2026). They may evolve into a variety of objects with related, but different characteristics, making identification ambiguous. The scarcity of LRDs at $z < 4$ also makes it difficult to answer the second question, as it limits our ability to study analogs in a regime where host galaxies would be more easily detected and used to inform the nature of their high-redshift counterparts.

In this paper, we will look at relatively low-redshift analogs both to learn more about the possible family tree of canonical LRDs and to see if they give hints on how to interpret the observations at higher redshift. LRDs have been identified at $z \lesssim 3$–4, extending this population to later cosmic times (e.g., I. Juodžbalis et al. 2024; R. Lin et al. 2025; M. Stepney et al. 2024; F. Loiacono et al. 2025; A. de Graaff et al. 2025a; Y. Ma et al. 2026; R. E. Hviding et al. 2026). Nonetheless, these discoveries are rare and no clear picture has emerged. Fortunately, rapid progress is being made to find larger samples. Using a thorough search of the SDSS database, X. Lin et al. (2026a) have identified three objects at $z \approx 0.1$ that match LRD properties closely (see also X. Ji et al. 2026). This is an important advance, but emphasizes how rare local close matches to canonical LRDs are. Furthermore, the search for low-z counterparts has recently been extended to the Dark Energy Spectroscopic Instrument (DESI; D. Collaboration et al. 2026) survey (see W. Ding et al. 2026; K. Park et al. 2026; X. Lin et al. 2026b).

Recently, J.-B. Billand et al. (2025) have explored the possibility that LRDs evolve by forming envelopes of young extended galaxies. To explore this possibility, they selected from a much larger sample of 55 red galaxies at $z_{med} = 3.6 \pm 1.1$ with such envelopes and derived their properties, concluding that these objects likely represent the next evolutionary step. However, their study does not explore alternative pathways: an important limitation, given the broad range of properties observed in canonical LRDs at high redshifts (see discussion in P. G. Pérez-González et al. 2026). That is, both their physical nature and, most importantly, their evolutionary fate at later cosmic times remain unclear.

In this paper, we discuss the missing link between canonical LRDs at high redshift and their counterparts at later cosmic times, namely objects potentially related to LRDs at $0.2 < z < 3.5$. Many of the proposed LRD analogs have been identified through JWST observations. It is important to note that, prior to JWST, the Spitzer mission (R. D. Gehrz et al. 2007) identified a variety of extragalactic sources in this redshift regime, the so-called Blue-excess Dust-obscured Galaxies (Blue HotDOG; R. J. Assef et al. 2016; A. Noboriguchi et al. 2022), which exhibit SEDs remarkably similar to those of LRDs as highlighted by A. Noboriguchi et al. (2023). Thus, they are a second good hunting ground for LRD analogs.

As part of the ongoing effort to bridge this gap, we have studied in detail WISEA J123635.56+621424.2 (here dubbed the Saguaro),[20] originally brought to prominence by Spitzer as an infrared-bright, optically faint galaxy (e.g., J. L. Donley et al. 2010). It is a well-studied object at $z = 2.0145$, located in GOODS-North (GOODS-N). It has an obscured AGN and a compact core in imaging from the Hubble Space Telescope (HST). Furthermore, its X-ray flux is very faint, indicating that it is Compton thick (CT) or nearly so (J. L. Donley et al. 2010). Data from the Near-Infrared Spectrograph (NIRSpec; P. Ferruit et al. 2022; P. Jakobsen et al. 2022) show the classical "V-shaped" feature at its core, similar to that seen in canonical LRDs. While its integrated SED differs somewhat from LRDs, its nuclear SED shows striking similarity, suggesting it may represent a more evolved descendant or an analog.

Notably, the Saguaro consists of a compact LRD-like nucleus *plus* a face on the spiral galaxy surrounding it. This provides an opportunity to explore whether, at high redshift, it would appear as a compact LRD, or whether it would be disqualified by the surrounding structure. We explore this question both by synthetically moving it to $z \approx 7$ and also by an analysis of the impact of surface brightness dimming on the detectability of LRD host galaxies in general.

This paper is organized as follows. In Section 2, we introduce the Saguaro and present its main observational characteristics. We then highlight its resemblance to canonical LRDs through three independent lines of evidence: (1) multiwavelength AGN–host image decomposition; (2) a spatially resolved NIRSpec/PRISM spectrum in its nuclear regions; and (3) a redshifting experiment illustrating how the system would appear if observed at higher redshifts. In Section 3, building on the findings from Section 2, we investigate, through stacking analysis, whether LRDs at $z \approx 4$–8 may similarly be embedded within faint extended emission that becomes increasingly suppressed with redshift due to cosmological surface brightness dimming. We then develop a simple analytic model quantifying the expected loss of detectable light from LRDs at increasing redshifts. In Section 4, we show that the Saguaro is not an isolated case. Finally, in Section 5, we discuss and summarize our findings.

Throughout this paper, we consider a cosmology with $H_0 = 70$ km s^{-1} Mpc^{-1}, $\Omega_M = 0.3$, and $\Omega_\Lambda = 0.7$. All magnitudes are total and refer to the AB system (J. B. Oke & J. E. Gunn 1983). As in A P. Kroupa (2001), the initial mass function (IMF) is assumed (0.1–100 $M_\odot$).

2. The Saguaro: A Case Study

The characteristic features of high-redshift LRDs are their "V-shaped" SEDs, typically emerging around the Balmer limit (D. J. Setton et al. 2025), and their compactness in NIRCam/F444W. They often show broad Balmer lines, commonly interpreted as evidence for active black hole accretion, although this interpretation remains actively debated. While this distinctive spectral shape has been predominantly observed at $z \gtrsim 3$–4, recent efforts have uncovered a few rare cases at lower redshifts (e.g., I. Juodžbalis et al. 2024; B. Wang et al. 2025c). We propose another intriguing example at $z \approx 2$: the Saguaro, located in the GOODS-N field (R.A. = 189.1482812, Decl. = 62.2400236), with an extensive multiwavelength coverage ranging from X-ray to submillimeter wavelengths.

In this section, we present the Saguaro and describe its general properties. We show that it has a "V-shaped" SED, which arises from the bright central core of the galaxy, based on a multiwavelength AGN–host image decomposition and a spatially resolved analysis of the NIRSpec/PRISM spectrum in its nuclear region. Finally, we investigate how this object would appear if observed at high redshifts, revealing a striking resemblance to canonical LRDs.

2.1. Dataset

We used both imaging and spectroscopic data from the GOODS-N field, obtained with the HST and JWST.

For HST, we relied on the Hubble Legacy Field (HLF) dataset, which provides broad wavelength coverage from 0.2 to 1.6 μm, including UV bands (WFC3/UVIS: F275W and F336W), optical bands (ACS/WFC: F435W, F606W, F775W, F814W, and F850LP), and near-infrared bands (WFC3/IR: F105W, F125W, F140W, and F160W). A detailed description is available in K. E. Whitaker et al. (2019).[21]

For JWST, we used both NIRCam and NIRSpec observations. NIRCam imaging was obtained from JADES/NIRCam Data Release 2 (DR2; PIDs: 1181; PIs: D. Eisenstein; D. J. Eisenstein et al. 2026, 2025; F. D'Eugenio et al. 2025),[22] complemented by data from the FRESCO program (PID: 1895; PI: P. Oesch; P. A. Oesch et al. 2023). These images reach 5σ depths of 29.3–29.9 mag (measured in 0.″15 radius apertures; see F. D'Eugenio et al. 2025 for more details on the data reduction). NIRSpec observations were obtained as part of the NIRSpec GTO WIDE survey (PID: 1211, PI: K. Isaak; M. V. Maseda et al. 2024). We made use of both PRISM and high-resolution data (G235H/F170LP and G395H/F290LP), the latter used to showcase the presence of a broad Hα and absorption feature in He I λ10830. For the PRISM observations, we primarily adopted the spectrum from the DAWN JWST Archive (DJA; see Sections 2.1 and 2.2.1). However, for the spatial analysis presented in Section 2.3.3, we used our own reduction of the PRISM data with MSAEXP[23] (v0.9.8; G. Brammer 2023). This dedicated reduction is used exclusively for that analysis, since the default nodding subtraction adopted in the DJA products can introduce self-subtraction effects that compromise a reliable spatial investigation of the nuclear region. The G235H/F170LP and G395H/F290LP data were fully reduced with MSAEXP from the outset.[24]

[20] In reference to the rare spiral-shaped crested Saguaros found in the Arizona desert; both are strikingly sculptural, with some of them being clearly spiral in form, and span impressive scales in their respective environments.

[21] HLF imaging is publicly available at https://archive.stsci.edu/prepds/hlf/.

[22] JADES images available at https://archive.stsci.edu/hlsp/jades.

[23] https://github.com/gbrammer/msaexp

[24] We note that Saguaro is covered by both G235H/F170LP and G395H/F290LP. However, both datasets are affected by cosmic rays and detector artifacts, and the limited number of exposures prevents their reliable use. Future high-resolution observations of this source will soon become available as part of PID 10311 (PIs: P. Rinaldi & E. Iani).

The Saguaro is also detected in the deep Chandra 2Ms X-ray data (Y. Q. Xue et al. 2016; ID: CDFN−190) with $L_{X,\,2-10\,\mathrm{keV,\ int}} = (6.61–10) \times 10^{43}\,\mathrm{erg\,s^{-1}}$ (J. L. Donley et al. 2010; A. Del Moro et al. 2016), with an absorbing column density of $N_{\mathrm{H}} \approx 10^{23.6-23.8}\,\mathrm{cm^{-2}}$ (D. M. Alexander et al. 2005; J. L. Donley et al. 2010). The source shows no detection in the Nuclear Spectroscopic Telescope Array (NuSTAR) data (F. A. Harrison et al. 2013). To validate the previous findings in the X-ray, we re-extracted and analyzed all the Chandra observations using the Chandra Interactive Analysis of Observations (CIAO; v4.17 and CALDB 4.11.0; A. Fruscione et al. 2006) tools (specextract). The spectra from different observations (covering a span of 1.5 yr) were combined in a single one via the CIAO tool combine_spectra. We did not find any significant variability in the covered time range. The object has an effective coverage of ≈1.96 Ms, with 246 net counts (i.e., background subtracted). Given the number of counts, we performed the spectral analysis using unbinned data and the *C*-statistic (W. Cash 1979). Due to the high background counts, we restricted our spectral fitting to rest-frame energies $E > 3.5$ keV, i.e., where the spectrum showed signal above noise. As the X-ray emission from the host galaxy (such as from X-ray binaries or supernovae remnants) is generally dominant only in the "soft" X-ray band ($E \leqslant 2$ keV, J. Wang & J. Y. Wei 2010), whereas the AGN emission dominates at $E > 2$ keV, we can safely assume that there should be no contamination by the host galaxy emission in the range of the spectrum we are fitting.

2.2. Properties of the Saguaro

We leveraged the available data for the Saguaro to construct a comprehensive picture of the system: (1) Section 2.2.1 outlines the host galaxy properties; (2) Section 2.2.2 examines the morphology; (3) Section 2.2.3 details its X-ray properties; and (4) Section 2.2.4 derives its $M_\bullet$ and discusses its implications.

2.2.1. Host Galaxy Integrated Properties

Figure 1 provides an overview of the Saguaro and the HST and JWST data used to derive its properties. Stellar masses of $\log_{10}(M_\star/M_\odot) \approx 11.3$ have been derived using the FAST code from M. Kriek & C. Conroy (2013) in the recent literature (R. P. Naidu et al. 2017; D. Liu et al. 2018; N. J. Cleri et al. 2023), often based on photometry compiled by R. E. Skelton et al. (2014). However FAST depends strongly on rest-frame optical colors, which for this galaxy are heavily contaminated by the infrared excess (see Figure 2). Therefore, to ensure the robustness of the previous measurements, we redetermined the galaxy mass using the AGN–host decomposition (see Section 2.3.2) to obtain the intrinsic stellar SED, as illustrated in Figure 3, and ran BAGPIPES (A. C. Carnall et al. 2019) for the synthesis modeling. We find $\log_{10}(M_\star) = 11.3 \pm 0.1$ (nominal uncertainties only). This confirms the previous values and appears to be inconsistent with the value of $\log_{10}(M_\star) \approx 10.46$ from A. Bongiorno et al. (2014).[25]

Previous works (e.g., J. L. Donley et al. 2010) suggest that the Saguaro hosts a deeply embedded AGN. To prove this, we selected the highest quality photometric measurements for this object from the recent literature to generate the SED shown in Figure 2 and listed in Table 1. We have decomposed the SED into two components: one according to a $\log_{10}(L_{\mathrm{IR}}/L_\odot) = 11.5$ LIRG template from G. H. Rieke et al. (2009) and the second as the remaining flux. The decomposition is nondegenerate for this case because of the extreme luminosity of the star-forming component, and the selected template is in agreement with the luminosity range found to fit the far-infrared of galaxies in this redshift range (W. Rujopakarn et al. 2013).

The strong emission from the very near-infrared to 5 μm of the remaining SED (see Figure 2) indicates the presence of a very deeply embedded AGN (i.e., CT or nearly so, e.g., A. Kirkpatrick et al. 2015; J. Lyu et al. 2024). We will find that its luminosity approximates the Eddington limit for the embedded SMBH (Section 2.2.4), indicating that little luminosity escapes. J. L. Donley et al. (2010) show that the mid-infrared spectrum is a virtually featureless power law rising rapidly toward longer wavelengths. Although some Hα escapes, the hydrogen lines are heavily obscured, as shown by Hβ not being detected. The source may be analogous to extreme objects like IRAS05189-2524 and IRAS08572+3915 (e.g., P. Severgnini et al. 2001; A. Efstathiou et al. 2014), deeply embedded AGNs with luminosities approaching 10^{12} $L_\odot$ but still letting sufficient light through to show AGN emission lines.

We can determine a star formation rate (SFR) from Figure 2. The total infrared luminosity from the star-forming template is 3.2×10^{12} $L_\odot$, corresponding to an integrated SFR of 500 $M_\odot\,\mathrm{yr^{-1}}$, consistent with the result from A. Bongiorno et al. (2014) but somewhat lower than some of the previous estimates (e.g., A. Del Moro et al. 2016; N. J. Cleri et al. 2023). The specific SFR (sSFR) is then $\approx 10^{-8.60}\,\mathrm{yr^{-1}}$, which is exceptionally high for its redshift, placing it along the upper envelope of the main sequence of star-forming galaxies (J. S. Speagle et al. 2014; P. Popesso et al. 2023). The luminosity of the AGN component is then 4.6×10^{12} $L_\odot$, assuming essentially all of it emerges in the infrared.

2.2.2. System Morphology

Figure 1 shows images of the Saguaro across the HST and NIRCam wavelength range. In the rest-frame UV, the emission is dominated by a compact central source surrounded by a faint halo, consistent with a face-on spiral host. As we move into the rest-frame optical, the extended galaxy becomes increasingly prominent (J. L. Donley et al. 2010). At redder wavelengths, the central core increasingly dominates the emission, as expected from the SED in Figure 2. This effect is visible across the individual bands (see Figure 1) and also in our AGN–host decomposition discussed later.

2.2.3. X-Ray Properties

To fit the X-ray spectrum, we chose a simple phenomenological model and a slightly more complex theoretical model. The phenomenological model is composed of a power law, a neutral absorber at the redshift of the source, and a local neutral absorber to correct for the Galactic absorption. Due to the redshift of the source and the limited amount of counts, our spectrum is limited to $E > 3.5$ keV, making it challenging to fit both the power-law slope and the source obscuration at the same time; therefore, we fixed the photon index to a canonical $\Gamma = 1.8$. The spectrum is well fitted by our simple model, and neither additional soft emission nor reflection components improve

[25] They already reported that the fit for this particular object was challenging (see their Section 4 and Figure 2).

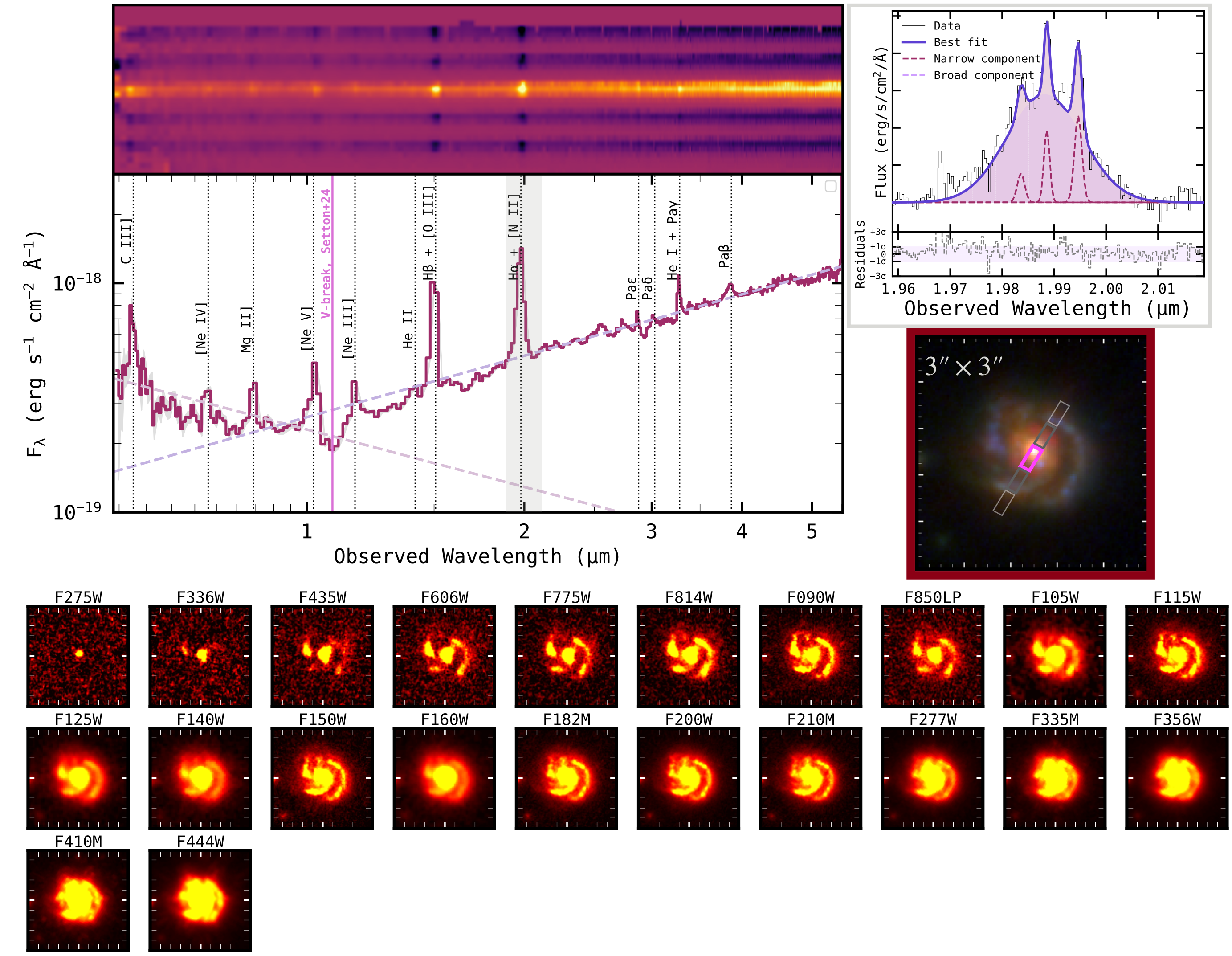

Figure 1. Top: on the left, we show the NIRSpec/PRISM spectrum of the Saguaro (from the DJA DAWN Archive; v4.4), with all prominent emission lines labeled. The expected position of the break, as defined by D. J. Setton et al. (2025), is marked in orchid. We also note the presence of [Ne IV]$\lambda\lambda$2422, 2424, as already reported in higher-z LRDs (see, e.g., M. Tang et al. 2026). The Hα + [N II]$\lambda\lambda$6548, 6583 complex (unresolved in the PRISM spectrum) is highlighted in gray. Its higher-resolution counterpart from the NIRSpec G235H/F170LP grating is shown in the top-right panel, along with the line model fits for both Hα and [N II] $\lambda\lambda$6548, 6583 (although we highlight the limited data quality of this dataset). Finally, we show the NIRCam RGB image (3″ × 3″) of the Saguaro with the slit overlaid, illustrating that the PRISM flux originates from the nuclear regions. Bottom: postage stamps (3″×3″) of the available HST and JWST filters for the Saguaro.

our fit significantly. Our fit provides an obscuration of $N_{\rm H} = (3.4^{+1.0}_{-0.8}) \times 10^{23}\,{\rm cm}^{-2}$ and an intrinsic (i.e., absorption-corrected) 2–10 keV (rest-frame) luminosity of $L_{2-10\,{\rm keV}} = (7.9^{+2.1}_{-1.6}) \times 10^{43}$ erg s^{-1}.

We tried to physically model the spectrum via the MYTorus model (K. D. Murphy & T. Yaqoob 2009), which self-consistently accounts for photoelectric absorption, Compton scattering, and fluorescent line emission in a toroidal geometry. MYTorus assumes a uniformly dense, toroidal obscurer with a fixed half-opening angle of 60°. This model can be used in both "coupled" and "decoupled" modes (T. Yaqoob 2012), the latter of which mimics a patchy/clumpy absorber, making it well suited for studying moderately to heavily obscured sources. We utilized MYTorus in its "coupled" configuration and, due to the low number of counts, certain parameters were fixed during fitting. Namely the slope at $\Gamma = 1.8$, and the scaling factors of the scattered continuum and line emission were both fixed at 1. We found results consistent with those from the phenomenological modeling, and obtained a torus obscuration along the line of sight of $N_{\rm H,los} \gtrsim 2.6 \times 10^{23}\,{\rm cm}^{-2}$, an inclination angle of $\geqslant$60°, and an intrinsic luminosity of $L_{2-10\,{\rm keV}} = (7.5^{+1.3}_{-1.1}) \times 10^{43}$ erg s^{-1}. All in all, our measurements are consistent with the previous literature (i.e., J. L. Donley et al. 2010; A. Bongiorno et al. 2014; A. Del Moro et al. 2016).

From our estimate of the intrinsic X-ray luminosity and using the infrared luminosity of the AGN component as $L_{\rm bol}$, we estimate the bolometric correction factor ($k_{\rm bol} \equiv L_{\rm bol}/L_{\rm X,2-10\,keV,int}$) to be $\approx$ 200. For an AGN of the appropriate luminosity, the expected value is $\approx$ 50 (F. Duras et al. 2020; C. Auge et al. 2023). This suggests that the intrinsic X-ray luminosity has been underestimated by as much as a factor of 4, or that the source is modestly X-ray weak.

As a check on this result, we have derived $L_{\rm bol}$ from [Ne V] λ3426, which can be used as a tracer of $L_{\rm bol}$ in obscured AGNs (e.g., R. Gilli et al. 2010; L. Barchiesi et al. 2024). We

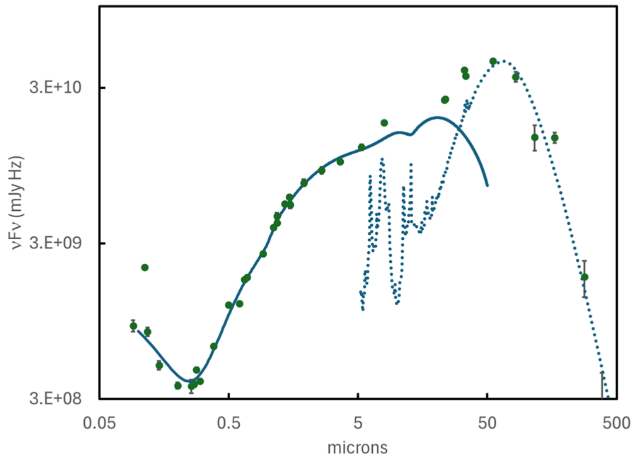

Figure 2. The rest-frame SED of the Saguaro. The template of a $\log_{10}(L_{\rm IR}/L_\odot) = 11.5$ star-forming LIRG (G. H. Rieke et al. 2009; dashed line) is fitted by least squares to the longest-wavelength data points from Table 1 ($\lambda_{\rm rest} > 80\ \mu$m) and subtracted from the total SED to isolate the nuclear component (solid line) after removing the star-forming contribution. This fit assumes that, over the fitted wavelength range, the AGN contribution is much smaller than the star-forming component, as generally observed in typical AGN SEDs (e.g., J. Xu et al. 2020; E. Bernhard et al. 2021; J. Lyu et al. 2022).

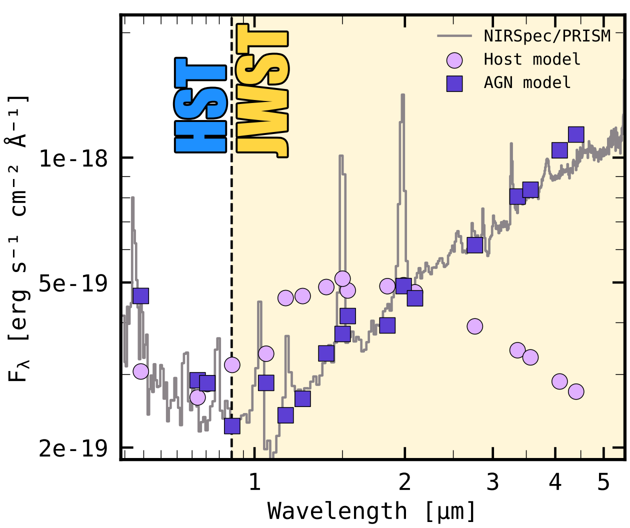

Figure 3. The NIRSpec/PRISM spectrum of the Saguaro at observed wavelengths (using the standard reduction from the DAWN JWST Archive), shown alongside the AGN–host decomposition photometry from GALFITM, scaled to match the NIRSpec/PRISM flux level at 2 μm. The vertical line indicates the transition from HST to JWST coverage, below which the UV photometry is provided solely by HST.

adopted the calibration presented in L. M. Feuillet et al. (2024)[26] (see their Section 4), where $(L_{\rm bol}/{\rm erg\ s^{-1}}) = 0.94\ \log_{10}(L_{[\rm Ne\ V]\lambda3426}/{\rm erg\ s^{-1}}) + 6.51$. We model the [Ne V] λ3426 line from NIRSpec/PRISM data with both MSAEXP and our internal pipeline (already used in P. Rinaldi et al. 2025b,a), obtaining a consistent flux of $(9.03 \pm 0.71) \times 10^{-17}$ erg s^{-1} cm^{-2}, corresponding to $L_{\rm bol} \approx (2.56 \pm 0.22) \times 10^{46}$ erg s^{-1}, where the uncertainty is driven primarily by the signal-to-noise ratio (S/N) of the line. The correlation itself is established at $\approx 4.5\sigma$ (L. Barchiesi et al. 2024), so the final estimate is $(6 \pm 1.5) \times 10^{12}\ L_\odot$, consistent with our result from integrating the infrared SED associated with the AGN.[27] This lends additional support to attributing this source component to an embedded AGN.

To further assess the X-ray nature of this source, we examine the relation between the rest-frame UV and X-ray monochromatic luminosities, $L_{2500\ \text{Å}}$ and $L_{2\ \rm keV}$, through the optical-to-X-ray index ($\alpha_{\rm OX}$; E. Lusso & G. Risaliti 2016). Without applying any dust correction to $L_{2500\ \text{Å}}$, we derive $\alpha_{\rm OX} \approx -1.25$. However, the interpretation of this value is not

Table 1
The SED Measurements of the Saguaro Compiled From the Literature, Corresponding to Those Shown in Figure 2

Rest-frame λ (μm)	νF_ν (mJy Hz)	Error (mJy Hz)	References
0.091	8.89E+08	7.42E+07	1
0.111	2.12E+09	3.61E+07	1
0.118	8.14E+08	5.37E+07	2
0.144	4.96E+08	3.23E+07	3
0.201	3.68E+08	1.70E+07	3
0.257	3.63E+08	3.63E+07	3
0.270	3.73E+08	1.49E+07	3
0.282	4.64E+08	8.50E+06	3
0.299	3.91E+08	3.33E+06	3
0.381	6.57E+08	2.09E+06	3
0.498	1.21E+09	2.60E+06	3
0.663	1.77E+09	2.38E+06	3
0.697	1.82E+09	2.14E+06	3
0.919	2.58E+09	2.17E+06	3
1.111	3.81E+09	1.90E+06	3
1.179	4.49E+09	2.25E+08	3
1.181	4.08E+09	1.58E+06	4
1.360	5.38E+09	2.20E+06	3
1.473	5.99E+09	1.86E+06	3
1.492	5.32E+09	2.66E+08	4
1.903	7.37E+09	3.69E+08	4
2.612	8.87E+09	4.43E+08	4
5.321	1.25E+10	5.61E+08	5
7.960	1.79E+10	5.24E+08	5
23.691	2.55E+10	3.40E+08	6
33.960	3.57E+10	9.23E+08	5
54.974	4.45E+10	1.48E+09	5
82.919	3.54E+10	2.63E+09	5
116.106	1.45E+10	2.69E+09	5
165.837	1.43E+10	1.09E+09	5
281.877	1.83E+09	4.80E+08	5
385.669	2.73E+08	1.68E+08	5

Note. References: (1) P. A. Oesch et al. (2018); (2) C. Borys et al. (2005); (3) M. J. Rieke et al. (2023b), JADES DR3 NIRCam photometry (GOODS-N v1.0; Extension 6) `circ0`, corrected to total flux (factor of 1.25); (4) H. I. Teplitz et al. (2011). All the IRAC measurements were reduced by a factor of 1.22 to bring them into agreement with the JADES photometry at similar wavelengths: this factor was determined by comparing the measurements at IRAC Band 1 and F356W; comparison of the model fluxes with the other IRAC bands showed a similar adjustment was needed for them; (5) D. Liu et al. (2018); (6) D. J. Hanish et al. (2015).

[26] Adapted from the calibration proposed in S. Satyapal et al. (2007) and rescaled to [Ne V]λ3426 as discussed in L. M. Feuillet et al. (2024).

[27] In contrast, N. J. Cleri et al. (2023) measured a [Ne V]λ3426 flux from HST/WFC3 G102 slitless spectroscopy that is nearly twice as large as our value. This difference is expected from the different spectral normalizations adopted. In this work, we rescale the spectrum to the model photometry of the central source, providing a measurement tied to the nuclear component. By contrast, the slitless measurement is tied to the total extracted light, for which the continuum normalization can include host-galaxy contribution. We therefore adopt our nuclear-normalized [Ne V] flux.

straightforward. The α_{OX} relation was calibrated primarily for unobscured AGNs, where the rest-frame UV emission is expected to be dominated by the accretion disk. This assumption may not hold for the Saguaro, since the observed rest-frame UV/optical light may include a contribution from the host galaxy and/or compact nuclear star formation.

At the same time, the source exhibits a high k_{bol} (≈200), suggesting that it may be X-ray faint relative to its inferred bolometric output. This apparent discrepancy may arise from residual X-ray absorption not fully accounted for by the applied column density, uncertainties in the inferred bolometric luminosity, contamination of $L_{2500\,\text{Å}}$, or an intrinsically weak X-ray corona. Reconciling the observed α_{OX} with a substantially more X-ray-weak regime would require additional attenuation, corresponding to $A_V \approx 2$ mag for a Calzetti reddening law (D. Calzetti et al. 2000). While this is slightly higher than the upper limit of A_V inferred from our BAGPIPES SED modeling, the values remain broadly consistent within the uncertainties and potential systematics in the SED decomposition.

The detection of broad Hα emission provides an additional, although not definitive, constraint on the obscuring geometry. It suggests that at least part of the broad-line region (BLR) remains visible along our line of sight. However, our X-ray modeling still indicates substantial obscuration, consistent with an inclined torus-like geometry. Therefore, broad Hα does not rule out residual X-ray obscuration. A natural interpretation is a partially obscured or patchy configuration, in which the BLR is not fully hidden while the more compact X-ray-emitting corona remains attenuated. Hβ cannot currently provide an independent test, as it is blended in the PRISM spectrum and is not covered by the available higher-resolution data. We therefore treat α_{OX} as an indicative, but not decisive, diagnostic for this source. A similar optical/X-ray mismatch was recently reported for the heavily obscured SMG ALESS073.1 at $z = 4.76$, where a very broad Hα component reveals the BLR despite a high X-ray column density close to the CT regime (E. Parlanti et al. 2024).

2.2.4. Properties of the SMBH

The Saguaro is covered by NIRSpec G235H/F170LP observations, which we reduced using MSAEXP. Its spectrum reveals a broad Hα component (see Figure 1) with $F(\text{H}\alpha) = (1.03 \pm 0.05) \times 10^{-16}\,\text{erg s}^{-1}\,\text{cm}^{-2}$ and an FWHM of $2521 \pm 256\,\text{km s}^{-1}$. We also detect the [N II]$\lambda\lambda$6548, 6583 doublet with a flux ratio of 3.01 ± 0.52, in agreement, within uncertainties, with the theoretical value of 3.05 (I. Dojčinović et al. 2023). The broad Hα was also found in previous works by A. M. Swinbank et al. 2004, A. Bongiorno et al. 2014, and G. D. Wirth et al. 2015.

Because of the uncertainties affecting the broad Hα measurement, including possible biases from residual cosmic rays and detector artifacts in the high-resolution data, the lack of high-resolution Hβ coverage needed to correct for dust attenuation, and the difficulty of isolating the intrinsic AGN continuum, we do not adopt an Hα-based black hole mass as our fiducial estimate. Instead, we estimate the black hole mass from the X-ray luminosity.[28] We follow the calibration from S. LaMassa et al. (2025). However, we need to correct for the very large k_{bol} (200) compared with the relation assumed there (E. Lusso et al. 2010). The result is $\log_{10}(M_\bullet/M_\odot) = 8.12$, with errors that are difficult to estimate because of the complexities in determining the intrinsic X-ray properties. This is consistent with the prior estimate of $\log_{10}(M_\bullet/M_\odot) = 7.99 \pm 0.3$ by A. Bongiorno et al. (2014), but is higher because of our allowance for the large k_{bol}. Thus, the resulting Eddington limit is $4.2 \times 10^{12} L_\odot$, essentially the same as our value for the AGN luminosity, i.e., the source is accreting close to the Eddington rate. The nucleus is broadly along the local $M_\bullet$–$M_\star$ relation (J. E. Greene et al. 2016) with $M_\bullet/M_\star \approx 0.0004$, i.e., within the scatter in that relation and the uncertainties in $M_\bullet$ and $M_\star$.

[28] Nonetheless, adopting the relation from A. E. Reines et al. (2013), we obtain a lower limit on $M_\bullet$ that is consistent with both literature estimates and our X-ray-based inferred value.

2.3. Resemblance to LRDs

In this section, we emphasize the similarity between the Saguaro and canonical LRDs by focusing on two defining features: its characteristic "V-shaped" SED (Section 2.3.1), which we show originates from the central region (Sections 2.3.2–2.3.3), the presence of a dense gas absorber in He Iλ10830 (Section 2.3.4), and the unresolved, point-like morphology it would present if observed at high redshift (Section 2.3.8). Moreover, we show that its submillimeter and X-ray detections, together with the presence of [N II] λ6548, 6583, do not contradict its resemblance to LRDs (Sections 2.3.5, 2.3.6, and 2.3.7).

2.3.1. The V Shape of the Saguaro

The NIRSpec/PRISM spectrum of the Saguaro provides one of the clearest examples of a "V-shaped" spectrum, emerging at a rest-frame wavelength comparable to those observed in canonical LRDs. We measure UV and optical slopes of −0.812 and 0.901 (see Figure 1), respectively. We find the spectrum is fully consistent with the definition of canonical LRDs proposed by D. D. Kocevski et al. (2025). We show these slopes in Figure 1. By adopting the same methodology as D. J. Setton et al. (2025), we find a spectral break at 3668^{+5}_{-28} Å, very close to the Balmer limit (3646 Å) as inferred by D. J. Setton et al. (2025) in their sample of LRDs. Interestingly, the "V-shaped" spectrum is observed in NIRSpec/PRISM data that sample nearly the central region of the galaxy, with the shutter positioned close to its nucleus.

2.3.2. Multiwavelength AGN–Host Image Decomposition

We further validate the "V-shaped" spectrum of the Saguaro using multiband photometric decomposition to separate the AGN from its host galaxy. We employ the GALFITM package (B. Häußler et al. 2013), an extension of the widely used GALFIT software (C. Y. Peng et al. 2002, 2010), to simultaneously model our NIRCam and HST images, allowing parameter variations as functions of wavelength. This method effectively leverages multiband data, producing more robust fits compared to single-band decompositions, while accounting for morphological wavelength variations. GALFITM has been widely utilized for structural decompositions of AGN–host galaxy systems at cosmic noon (e.g., M.-Y. Zhuang & L. C. Ho 2023; M. Zhuang et al. 2023; S. Gillman et al. 2025).

We model the AGN as a point source and the host galaxy with a single Sérsic profile to capture its dominant structure (see Figure 10 in the Appendix). While the host exhibits spiral arms, they are far enough from the galactic center that they do not contaminate the AGN flux significantly. Our Sérsic model thus represents the azimuthally averaged light profile of the disk. A more complex decomposition, incorporating a galactic bar and a nearby stellar clump, located 0.″18 southwest of the nucleus, is presented later in this section (see Figure 11 in the Appendix). However, we adopt the simpler AGN–galaxy decomposition as our fiducial result, since it captures the dominant components while avoiding parameter degeneracy associated with more complex models. We do not include a bulge component, as neither the NIRCam nor HST images reveal a prominent bulge component. If present, the bulge is likely a pseudobulge; classical bulges typically have effective radii larger than 1 kpc (P. Dimauro et al. 2019), which would be resolved by NIRCam. For example, the FWHM of the NIRCam/F200W point-spread function (PSF) is 0.″064, corresponding to 0.55 kpc at $z = 2$, smaller than the typical radius of a classical bulge. Pseudobulges generally have bulge-to-total flux ratios below 0.2 (D. B. Fisher & N. Drory 2008), and since the Saguaro is brighter than its host in most bands, any contribution from a pseudobulge is likely minor.

In the GALFITM configuration, we use Chebyshev polynomials to model the wavelength dependence of structural parameters, allowing for smooth variation across filters while mitigating overfitting. The magnitudes of both the AGN and Sérsic components are left free in all bands. The Sérsic index and half-light radius are allowed to vary quadratically with wavelength, following the approach of B. Häußler et al. (2013) and M. Zhuang et al. (2023), which provides sufficient flexibility to capture real structural changes while maintaining stability in low signal-to-noise filters. To avoid introducing artificial wavelength-dependent distortions, we fix the ellipticity and position angle across all bands. We also assume the AGN and host galaxy share a common center, fixed in all bands. Nearby galaxies are manually masked in the decomposition.

We present our results in Figure 3, which shows the modeled photometry for both the host galaxy and the AGN, each normalized to match the NIRSpec/PRISM spectrum at 2 μm, along with the spectrum itself. The AGN–host decomposition reveals that the characteristic "V-shaped" SED is well reproduced by the point-like source used to model the AGN component, distinct from the SED of the host galaxy. As a test, we also estimated the relative AGN and host contributions as a function of radius (see Figure 12 in the Appendix). We find that the AGN component dominates at small radii, while the host contribution becomes dominant at larger radii. If one considers the standard LRD criteria (see P. Rinaldi et al. 2026 for an overview), Saguaro would not be robustly selected as an LRD. First, classical color cuts based on fixed observed-frame filters (see, e.g., I. Labbé et al. 2023; G. Barro et al. 2024a) are not ideally suited to Saguaro because, at its redshift, they do not probe the useful rest-frame wavelength ranges. A more appropriate alternative is the criterion proposed by D. D. Kocevski et al. (2025), which adopts a bandpass-shifted approach. By exploring different apertures, from 0.″1 to 0.″6, we find that only the smallest aperture, i.e., 0.″1, satisfies the color selection. More critically, Saguaro fails the compactness requirement, since the source is resolved in F444W (when host and AGN are not separated). This is also why it was not included in the recent, more inclusive census of LRDs by P. Rinaldi et al. (2026). These results show that lower-z LRD analogs with prominent host emission may be missed by standard selections, and that identifying such systems may require separating the compact nuclear component from the extended host contribution. A similar conclusion has also been suggested recently by J.-B. Billand et al. (2025).

The host galaxy properties are consistent with normal disk galaxies. The half-light radius of the host galaxy is 5.8 kpc at rest-frame 0.15 μm and decreases to 3.7 kpc at 1.5 μm, consistent with the known trend of decreasing size with wavelength (e.g., B. Vulcani et al. 2014). The measured Sérsic index remains near $n \approx 1$ across all bands, typical of disk galaxies. The SED of the host galaxy, as shown in Figure 3, resembles that of normal spiral galaxies in the local universe (M. J. I. Brown et al. 2014), showing a Balmer break and a downturn beyond ≈2μm (rest-frame 0.7 μm), in contrast to the steeply rising AGN SED. In the rest-frame UV, the F_λ decreases with wavelength, but the slope is flatter than that of the AGN.

Interestingly, residuals near the galaxy center reveal asymmetric, off-center features located ≈0.″1 (≈0.8 kpc) from the nucleus. This structure is unlikely to be a bulge given its offset from the nucleus. It resembles the off-center blobs seen in LRDs by C.-H. Chen et al. (2025), which they suggest might be merging companion galaxies, disturbed host structures, or AGN-illuminated nebular emission. Notably, the Saguaro has two neighboring galaxies to the east and southeast at projected distances of 24 and 26 kpc. Their JADES photometric redshifts from the JADE catalog are 2.04 and 2.03, respectively, consistent with the spectroscopic redshift of the Saguaro ($z = 2.0145$), suggesting potential physical association. If spectroscopically confirmed, they could possibly be evidence of ongoing minor mergers. Alternatively, the asymmetric, off-center features could also be a stellar clump near the nucleus, which is commonly seen in $z \approx 2$ galaxies (e.g., B. S. Kalita et al. 2024).

Finally, we tested a sophisticated model including a bar and a stellar clump in the modeling, fitted alongside the AGN and disk. The clump, located 0.″18 southwest of the nucleus, is clearly seen in short-wavelength images. The bar, oriented northeast–southwest, is most prominent at long wavelengths, likely due to relatively older stellar populations common in bars. The bar is modeled with a Sérsic profile with a center tied to the disk. The fluxes across multiple bands are allowed to be free, while the Sérsic and radius are allowed to vary quadratically with wavelengths. The stellar clump is modeled as a point source. We find an improvement in residuals, and the AGN SED retains its V shape. However, the added complexity introduces degeneracies and unphysical wiggles. For example, in the F200W band, where the bar is not visible, the model increases bar flux to account for the asymmetric, extended feature mentioned above, and thus reduces the inferred AGN flux. Moreover, at long wavelengths, the stellar clump is blended with the AGN due to lower resolution. To avoid such artifacts, we adopt the simpler AGN–Sérsic decomposition as our baseline. The sophisticated model confirms that contamination from the substructures is <10%, so it does not affect our main conclusions.

Although the AGN–host decomposition reveals the spatial coincidence of the AGN with the observed "V-shaped" SED feature, it remains unclear whether it arises solely from AGN activity or is also influenced by an additional component, such as hot, young stars in a circumnuclear starburst ring. These structures are commonly observed in the central regions of active galaxies at low redshift ($z \lesssim 0.1$). Although they have typical radii $\gtrsim$0.5 kpc (e.g., J. K. Kotilainen et al. 2000; T. Bohn et al. 2023), which would be resolved with NIRCam at the redshifts probed here ($z \approx 2$), it remains uncertain whether similar structures exist on smaller, unresolved spatial scales. In this regard, ALMA observations have revealed a more complex picture in the nuclear regions of high-z galaxies, often showing clumpy, compact star formation and gas distributions (e.g., R. Gilli et al. 2014; J. A. Hodge et al. 2019), which may cause contamination to our AGN-only SED at rest-frame UV and blue-optical SED, i.e., roughly $\approx$0.12–0.4 μm (e.g., R. M. González Delgado & T. Heckman 1999).

2.3.3. The "V Shape" Lives at the Center of the Galaxy: Insights From NIRSpec/PRISM

The multiwavelength AGN–host image decomposition revealed that the "V-shaped" SED arises primarily from the AGN component used to model the central source. To investigate this detail, we further analyzed the NIRSpec/PRISM observations, which cover the central region of the object (see Figure 1). In particular, we performed an ad hoc reduction of the NIRSpec/PRISM data using MSAEXP. However, instead of the default nodding technique (adopted by the DAWN JWST Archive), which can suppress extended emission in the outskirts, we applied a customized background subtraction method following the procedure described in A. de Graaff et al. (2025c), now fully implemented in MSAEXP. In this approach, a global master sky spectrum is subtracted rather than using image differencing, effectively avoiding self-subtraction and preserving any extended structure. This strategy is essential to determine whether the "V-shaped" feature is truly concentrated in the nuclear region of the Saguaro, as it maximizes the recovered flux across the entire spatial profile.

By preserving the full spatial structure in the 2D spectrum and avoiding the background suppression due to default nodding techniques, we were able to extract one-dimensional spectra at each spatial pixel along the cross-dispersion axis, including those just beyond the nuclear regions of the galaxy. As described in the previous section, the AGN–host decomposition performed with GALFITM provided photometry for both the compact central AGN and the more extended host component. Therefore, for each spatial row, we compare the extracted spectrum with the corresponding AGN–host decomposed photometry, normalized at 2 μm.

We show the extracted spectra in Figure 4. While this analysis pushes the NIRSpec/PRISM data to its limits, it clearly reveals a strong contrast between the central "V-shaped" SED and the surrounding regions. The characteristic "V shape" is most prominent within the central $\approx 0\overset{\prime\prime}{.}1$–$0\overset{\prime\prime}{.}2$ (corresponding to $\approx$0.8–1.5 kpc at $z = 2.0145$). To explore this, we fit the spectrum extracted in each row as a linear combination of the AGN and host components derived from the GALFITM decomposition. This provides a quantitative estimate of the relative AGN and host contributions as a function of distance from the center. We find that the "V-shaped" component dominates in the central row, but is rapidly diluted at larger radii, where the host emission becomes dominant.

Although the NIRSpec/PRISM spectrum provides spatial information along the slit direction, the row-by-row extractions should not be interpreted as independent measurements at the native $0\overset{\prime\prime}{.}1$ pixel scale. The effective spatial resolution is set by the NIRSpec PSF, which redistributes nuclear light into adjacent rows. Therefore, the transition observed in the extracted spectra should be regarded as PSF smoothed rather than spatially sharp. With this caveat, we still find a coherent spatial trend. The central rows show the strongest "V-shaped" continuum, while at offsets of order $\approx 0\overset{\prime\prime}{.}1$–$0\overset{\prime\prime}{.}2$ and beyond this component becomes progressively diluted and the spectrum increasingly resembles the host-dominated component inferred from the independent GALFITM decomposition. This supports the conclusion that the "V-shaped" SED is mainly associated with the innermost region of the galaxy.

These findings also underscore the importance of slit placement when attempting to identify such features from spectroscopy alone. The presence and detectability of a "V-shaped" SED in a spectroscopic extraction could strongly depend on whether the aperture or shutter covers the compact nuclear component. This is particularly relevant when the imaging data do not have sufficient S/N or resolution to enable a reliable image decomposition. In such cases, slight slit or shutter misalignments could dilute or miss the nuclear component, potentially hiding "V-shaped" cores within otherwise normal-looking galaxies.

2.3.4. The Presence of Dense Gas Absorber in the Saguaro

Recent models suggest that the peculiar spectra of LRDs cannot be explained by a standard BLR alone. Instead, they may be shaped by radiative-transfer effects through dense, partially ionized, high-column-density gas around the central source, producing their distinct features, including Balmer absorption (e.g., A. de Graaff et al. 2025a; K. Inayoshi & R. Maiolino 2025; X. Ji et al. 2025; R. P. Naidu et al. 2025). Nonetheless, a similar absorption feature can also appear in He Iλ10830, which provides a complementary tracer of dense, partially ionized gas because it arises from the metastable 2^3S level and does not require the extreme population of the short-lived H($n = 2$) level needed for Balmer absorption.

Therefore, we searched for similar absorption features in the high-resolution spectra covering the Saguaro. We stress that this inspection is strongly limited by the relatively poor data quality, and defer a more detailed analysis to a future paper based on higher-quality NIRSpec/IFU data from PID 10311. Nonetheless, this search remains informative, as it allows us to assess possible similarities and differences with respect to what is commonly observed in canonical LRDs.

First, we do not identify any clear absorption feature in Hα (see Figure 1). Whether this reflects the intrinsic absence of Balmer absorption or is simply due to the limited data quality remains unclear. However, in the G395H/F290LP spectrum, both the 2D and 1D data show evidence for an absorption feature associated with the He Iλ10830 line (see Figure 5). This feature appears as a strongly blueshifted absorption component superimposed on the overall emission-line complex, together with broad Pa-γ emission.

Our fit strongly favors a model including the absorption component. Specifically, we find $\Delta_{\rm BIC} > 100$ relative to a model without absorption, corresponding to an $\approx 5\sigma$ detection. Following the methodology outlined in F. Loiacono et al. (2025), we infer a velocity offset of $\Delta v = -885.2 \pm 36.5$ km s^{-1} and an

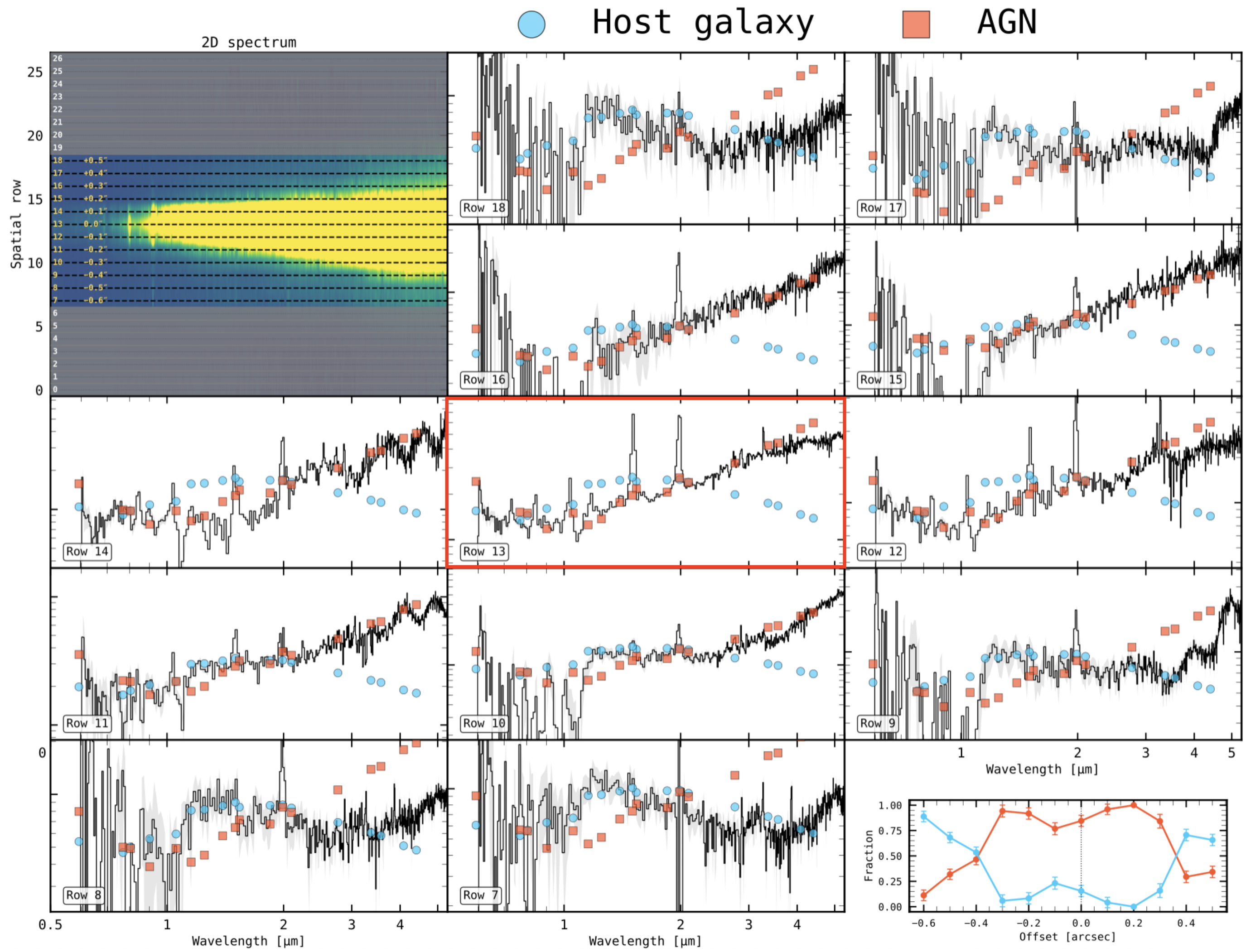

Figure 4. Extraction of row-by-row 1D spectra from the NIRSpec/PRISM 2D data of the Saguaro. Spectra are shown in F_λ (y-axis) versus λ (x-axis); spectra are shown in the observed frame. Each subplot on the right shows the extracted spectrum (black) for a given spatial row, along with the corresponding host galaxy and AGN photometry (from GALFITM) normalized (at 2 μm) to match the extracted spectrum at each row. The center of the trace is located at row 13 (highlighted in red). We also report the distance from the center of the spectral trace. We fit the spectrum extracted in each row as a linear combination of the AGN and host components inferred from the GALFITM decomposition. This allows us to estimate the relative AGN and host contributions as a function of distance from the center. We find that the "V-shaped" component dominates in the central row, but becomes diluted at larger radii, where the host contribution takes over.

FWHM of 634.3 $\pm$ 84.2 km s^{-1}. The corresponding column density of helium in the metastable 2^3S level is $N(\mathrm{He\,I}\,2^3S) \approx (1.73\text{–}2.50) \times 10^{13}$ cm^{-2}.

Although Hα absorption is commonly observed in canonical LRDs, the situation observed in the Saguaro (namely, the absence of clear Hα absorption together with the detection of He Iλ10830 absorption) is not unique. A similar combination has also been reported in J1047 (X. Lin et al. 2026a; local LRD analog) and GLIMPSE-17775 (V. Kokorev et al. 2026; a $z = 3.501$ LRD), showing that this combination is present in other claimed LRDs or LRD analogs.

2.3.5. The Submillimeter Flux

The current strong submillimeter flux seen in the Saguaro is clearly in violation of the properties of canonical LRDs (C. M. Casey et al. 2025). However, as shown in Figure 2, this is completely driven by the very high rate of star formation, which is likely to deplete the interstellar gas and fade quickly ($\lesssim$ 20 Myr) (e.g., N. M. Förster Schreiber et al. 2003) with an upper limit of 20–60 Myr set by the gas depletion timescale (F.-Y. Liu et al. 2024). This could leave a dust-enshrouded AGN that emits weakly in the submillimeter flux (unless it has successfully blown away its cocoon). In any case, ULIRGs and high Eddington ratio AGNs are not strongly correlated (G. H. Rieke et al. 2025), so this source component does not seriously undermine the analogy with LRDs.

2.3.6. The X-Ray Detection

Recent studies have shown that LRDs are notoriously faint in the X-ray regime. In most cases, X-ray data do not yield individual detections, and stacking analyses have only provided upper limits (e.g., T. T. Ananna et al. 2024; M. Yue et al. 2024). This has led to the interpretation that LRDs are, on average, intrinsically X-ray weak, heavily obscured, or both. In this context, the X-ray luminosity inferred for the Saguaro ($\log_{10}(L_{2-10\,\mathrm{keV}}/\mathrm{erg\ s^{-1}}) = 43.88 \pm 0.07$) lies at the upper end of the existing upper limits (spanning $\log_{10}(L_{2-10\,\mathrm{keV}}/\mathrm{erg\ s^{-1}}) \approx 42.5\text{–}44.5$; see Figure 1 in M. Yue et al. 2024). A

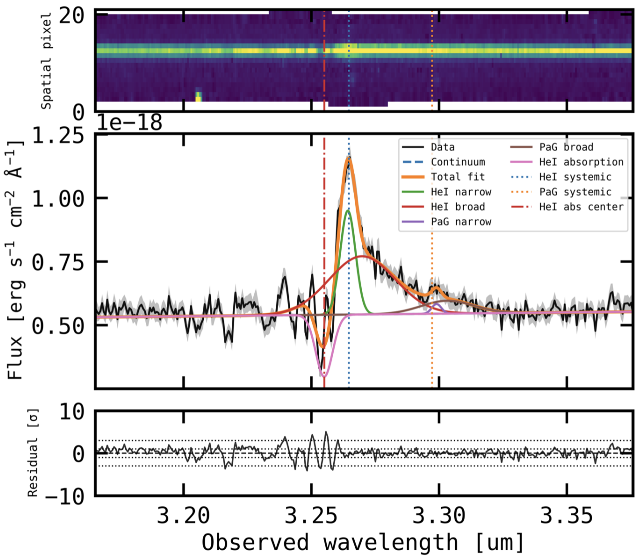

Figure 5. G395H/F290LP spectrum covering the He Iλ10830 and Pa-γ emission-line complex. A clear absorption feature is visible in both the 2D and 1D spectra, indicating the presence of dense neutral or partially ionized gas along the line of sight, likely located in the nuclear region close to the accretion disk and/or the BLR.

few confirmed X-ray-detected LRDs (XRDs) are currently known, though. D. D. Kocevski et al. (2025) reported two cases: PRIMER-COS 3866 at $z = 4.66$, with $\log_{10}(L_{2-10\,\mathrm{keV}}/\mathrm{erg\ s^{-1}}) = 44.7 \pm 0.2$, and JADES 21925 at $z = 3.1$, with $\log_{10}(L_{2-10\,\mathrm{keV}}/\mathrm{erg\ s^{-1}}) = 43.73 \pm 0.06$. The former is substantially more X-ray luminous than the Saguaro, while the latter is comparable. More recently, R. E. Hviding et al. (2026) reported another prominent XRD, with an X-ray luminosity comparable to PRIMER-COS 3866 but at lower redshift ($z \approx 3.28$).

Therefore, although the X-ray detection of the Saguaro may appear exceptional at first glance, it instead places the source among the rare XRDs currently known. Moreover, our analysis suggests that the Saguaro is both X-ray weak and strongly obscured, as indicated, for example, by its high bolometric correction ($k_{\mathrm{bol}} \approx 200$). We therefore conclude that its X-ray detection does not contradict its resemblance to the LRD population. Rather, as discussed for XRD (R. E. Hviding et al. 2026), the Saguaro may represent a transitional object, further strengthening its role as a key system for investigating the eventual fate of LRDs at later cosmic times.

2.3.7. The Presence of [N II]λ6548, 6583 in the Saguaro

Another apparent difference between the Saguaro and classical LRDs at higher redshift is the clear presence of [N II]λ6548, 6583, which has not been commonly reported in classical high-z LRDs. One could argue that this feature weakens the comparison between the Saguaro and the high-redshift LRD population. However, recent DESI results (D. Collaboration et al. 2026) have revealed LRD-like systems at $z < 1$, where both weak and strong [N II]λ6548, 6583 emission has been reported (see W. Ding et al. 2026; X. Lin et al. 2026b; K. Park et al. 2026). In particular, W. Ding et al. (2026) reported five LRD-like systems at $z \approx 0.2$–0.4 whose spectral shapes closely resemble those of classical high-z LRDs. Similar to the Saguaro, these systems also show relatively strong [N II] emission, with line ratios comparable to those measured in the Saguaro ($\log_{10}([\mathrm{N\,II}]/\mathrm{H}\alpha) \approx 0.05 \pm 0.05$). The presence of [N II] therefore does not necessarily rule out a connection with the classical LRDs. Instead, it may indicate that the Saguaro, and other systems with comparable [N II]/Hα ratios, are more chemically evolved than classical high-z LRDs, which are likely hosted by low-metallicity systems. This could reflect their more prominent host-galaxy contribution and a more advanced evolutionary stage. Consistently, both the Saguaro and the DESI LRD-like systems from W. Ding et al. (2026) lie on the local $M_{\bullet}$–$M_{\star}$ relation, suggesting that they may represent later evolutionary stages of compact, rapidly accreting systems observed at much higher redshifts, in which the host galaxy has caught up with the growth of the central supermassive black hole. Finally, visual inspection of the recently reported low-z LRDs from DESI (W. Ding et al. 2026; X. Lin et al. 2026b; K. Park et al. 2026) shows that these systems are often embedded within extended galaxies. This further suggests that some apparent contradictions may arise from the stronger contribution of the host galaxy in these systems compared to their classical high-z counterparts.

2.3.8. How We Wonder What you Would Have Looked Like in the Early Universe

We showed that the Saguaro exhibits a "V-shaped" spectrum originating from its nuclear region, with the "V-break" occurring at the characteristic wavelength reported in the literature (D. J. Setton et al. 2025). We then demonstrated that AGN–host image decomposition confirms the spatial coincidence of this spectral shape with the central AGN as well as the presence of a dense gas absorber in the Saguaro. Finally, we highlighted that its submillimeter flux, X-ray detection, and the presence of [N II]$\lambda\lambda$6548, 6583 do not violate its resemblance to the broader LRD population. This strong resemblance to LRDs naturally raises the question of whether this object represents a low-redshift analog of LRDs. However, some key differences must be taken into account. First, compactness is a defining characteristic of LRDs, whereas our object (considering both AGN and host) is clearly extended. Second, the Saguaro is observed at $z \approx 2$, while canonical LRDs are typically observed at $z \gtrsim 4$–5. Additionally, its face-on disk morphology and far-infrared properties differ significantly from what is currently known about LRDs (although the latter may be a transient phase). Furthermore, the prominent [N II] emission in the Saguaro may indicate a host galaxy that is more chemically enriched and massive than those typically associated with canonical LRDs. These differences could reflect evolutionary changes over cosmic time.

This ambiguity makes a compelling case for investigating whether it can be considered as a possible analog of canonical LRDs at later epochs. Therefore, we investigate how the Saguaro would appear if observed (unchanged in its intrinsic properties) at higher redshifts. We emphasize that this is a simplified, toy experiment. Nevertheless, this exercise raises important questions about whether current observations of LRDs at high redshift are systematically biased in recovering host galaxy properties, as recently suggested by F. Pacucci & A. Loeb (2025) and J.-B. Billand et al. (2025). In this regard, P. Rinaldi et al. (2025a) have already shown that approximately 30% of photometrically selected high-redshift LRDs exhibit complex or disturbed

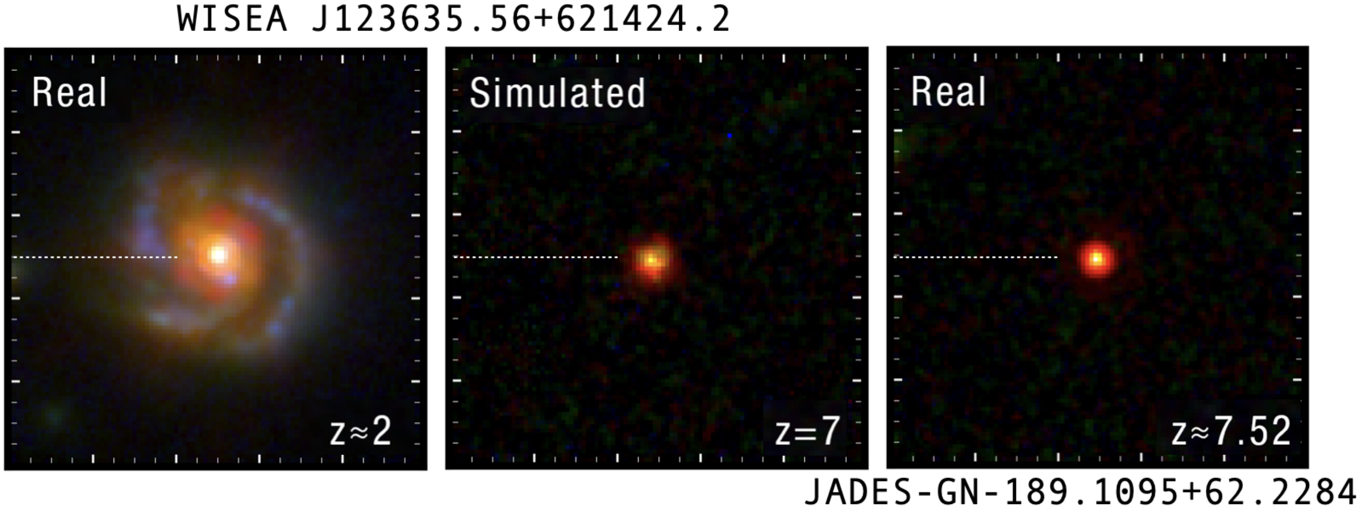

Figure 6. Visual demonstration of cosmological surface brightness dimming and its impact on the host galaxy. Left: the real Saguaro (WISEA J123635.56 +621424.2) observed at $z = 2.0145$. Center: the same galaxy artificially redshifted to $z = 7$ using the FERENGI prescription (M. Barden et al. 2008). Right: a representative LRD at comparable redshift from P. Rinaldi et al. (2025a). All cutouts are $3'' \times 3''$. The toy experiment demonstrates how the host galaxy becomes increasingly suppressed in its outskirts, while the central regions remain detectable, mirroring the effect observed in LRDs. For these RGB images, we make use of the code TRILOGY (D. Coe) with some customized steps. Briefly, each band is independently scaled using a sigma-clipped estimate of the background and a logarithmic stretch. This scaling is designed to suppress noise-dominated pixels (and thus equalize the background across all images), preserve faint extended emission, and avoid excessive saturation of the brightest regions. The RGBs are based on F444W, F277W, and F090W.

morphologies (which they interpret as a proxy for merger activity in at least a subset of LRDs), underscoring the need to carefully consider observational limitations, such as image depth, which might bias this fraction.

To investigate how cosmological surface brightness dimming (R. C. Tolman 1930) affects the detectability of extended emission in the Saguaro at high redshifts, we performed pixel-by-pixel SED fitting using EAZYPY (G. B. Brammer et al. 2008). The redshift was fixed to that of the galaxy derived from the NIRSpec/PRISM spectrum. We adopted the `BLUE_SFHZ_13` template set along with an AGN+torus template, which includes redshift-dependent star formation histories and dust attenuation. In particular, the AGN+torus template is based on the NIRSpec/PRISM spectrum of the $z = 4.50$ source from GO-1433 in the MACS0647 field (PI: D. Coe; see M. Killi et al. 2024). This source exhibits a spectral shape representative of LRDs, and therefore it is useful to describe the nuclear region of the Saguaro. The fit was restricted to NIRCam bands only, taking advantage of their superior spatial resolution. All bands were PSF matched to F444W using STPSF (M. D. Perrin et al. 2014), and SEDs were extracted from each pixel after masking nearby contaminants.

Each pixel's SED was then redshifted to the target redshift, and the galaxy's appearance at earlier cosmic times was reconstructed following a FERENGI-like methodology (M. Barden et al. 2008). This includes angular size rescaling using the proper angular diameter distance ratio, full $(1 + z)^{-4}$ surface brightness dimming, and bandpass shifting. An evolutionary brightening term was also applied (see next paragraph). The redshifted SEDs were projected onto a blank canvas, convolved with the corresponding PSF, and injected into a real background extracted from a region close to the source. The background was cleaned by masking sources and replacing contaminated regions with nearby noise samples to preserve realistic structure and depth.

We stress that for this toy experiment, our goal is purely to visualize how cosmological surface brightness dimming affects the extended host galaxy. To that end, we adopt the phenomenological prescription implemented in FERENGI, applying a uniform brightening of $M_{\rm evo}(z) = x\,z + M_0$ with $x = -1$ (M. Barden et al. 2008). Following the discussion in M. Barden et al. 2008, this choice is made purely for visual purposes, to illustrate the impact of surface brightness dimming with redshift. We note that a physically realistic treatment would require evolving the AGN and host components separately, with the AGN scaled according to the evolution of the quasar bolometric luminosity function (e.g., X. Shen et al. 2020; H. Zhang et al. 2024), and the host following the stellar mass-to-light evolution observed in star-forming galaxies (e.g., T. Treu & L. V. E. Koopmans 2004).

We show the results of this toy experiment in Figure 6, which showcases three RGB images: the real object (on the left), its simulated appearance at $z = 7$ (at the center), and, for comparison, a representative LRD at similar redshift (on the right). This experiment demonstrates how cosmological surface brightness dimming preferentially suppresses low-surface-brightness emission in galaxy outskirts while leaving compact central components detectable. This differential effect, which is consistent with the findings of V. Calvi et al. (2014), highlights how extended stellar light can easily fall below detection thresholds at high redshift, potentially explaining the lack of extended host galaxies around LRDs as redshift increases.

3. How Much We Never See: Are LRDs Embedded in Extended Hosts?

3.1. The Stacked UV Profile of LRDs

We showed that the Saguaro (1) exhibits a "V-shaped" SED at its center, as revealed by both the AGN–host decomposition and the spatially resolved NIRSpec/PRISM spectrum, and (2) that if redshifted to high redshift (unchanged in its properties), the cosmological surface brightness dimming would preferentially suppress flux from the outskirts, leaving only the central

AGN visible. Given the striking resemblance between the Saguaro and LRDs, and taking into account the intrinsic size evolution of galaxies with redshift (e.g., K. Ormerod et al. 2024; A. Genin et al. 2025), this naturally raises the question of whether observational biases significantly affect our current view of canonical LRDs at high redshift.

To explore this possibility, we analyzed the sample of 99 photometrically selected LRDs at $z \approx 4$–8 presented in P. Rinaldi et al. (2025a), noting that not all of them necessarily host an AGN[29]. We stacked all sources using filters probing the rest-frame UV range of 1500–2000 Å (F090W, F115W, and F150W) after PSF-matching each image with STPSF to the reddest available filter in that wavelength range (F150W). Median-stacked cutouts were centered on the LRD positions, enhancing coherent low-surface-brightness features while suppressing outliers. To ensure that the stack captures only emission associated with the LRDs, all sources beyond $0''.3$ from the center were masked out prior to stacking. This method enables the isolation of extended UV emission.

We then derived the radial surface brightness profile of the stacked image and compared it to two PSF references: (1) the nominal PSF used for matching (F150W), and (2) a simulated stacked PSF created by repeating our full stacking procedure on synthetic NIRCam PSFs.[30] To ensure realism, we applied random V3-angle rotations and spatial offsets before stacking, mimicking the astrometric and orientation variations present in the real dataset. We randomly applied a 1 pixel shift along both the x and y directions, corresponding to 30 mas for the NIRCam short-wavelength channel. No measurable systematic dependence is found on the V3 angles, while the results are strongly sensitive to the applied offset. In particular, the 30 mas shifted PSF is broader than the nominal PSF by a factor of $\approx$2–3 at $r \approx 0''.05$, increasing to $\approx$3–5 at $r \approx 0''.1$–$0''.3$, as one can see in Figure 7. In our case, the applied offset is deliberately exaggerated, being approximately 6 times larger than the typical internal astrometric scatter in the JADES images ($\lesssim$5 mas), and was adopted to estimate a conservative upper limit on the impact of residual astrometric uncertainties on the inferred extended host UV emission associated with LRDs.

Figure 7 (on the left) shows the result assuming a conservative background subtraction, where the outermost profile points are not allowed to average negative. Figure 7 (on the right) applies a more aggressive subtraction,[31] allowing for negative values in the outskirts. In both cases, significant excess emission is seen beyond the PSF, extending to a radius of $\approx 0''.2$, or $\approx$2–3 kpc in diameter. The agreement between the two profiles down to a normalized intensity of 10^{-2} supports the robustness of this detection. This is also consistent with the recent findings of X. Lin et al. (2024), who analyzed a sample of broad Hα emitters at $z \approx 4$–5. However, their sources were not explicitly selected as LRDs and were drawn from a significantly smaller sample, yet the results are similar.

Interestingly, we repeated the same stacking analysis using only the subset of LRDs with spectroscopic redshifts (26 galaxies in total). Although this subset represents a modest fraction (approximately 26%) of the full sample, the results remain unchanged, even when applying aggressive background subtraction (see Figure 13 in the Appendix). We also repeated the experiment excluding the galaxies classified as having "complex UV morphology" in P. Rinaldi et al. (2025a), and found consistent results, further supporting the idea that canonical LRDs may reside within extended, low-surface-brightness envelopes. A similar result has also been reported for the optical emission; indeed, Y. Zhang et al. (2025) found evidence for a host component through a stacking analysis of more than 200 LRDs in COSMOS-Web, further supporting the presence of a faint extended host emission in LRDs.

Moreover, when examining the stacked images in successive redshift bins[32] ($z \approx 4$–5.8, $z \approx 5.8$–7, $z \approx 7$–8), we observe a slight evolution in the extent of the radial profiles from $z \approx 7$–8 to $z \approx 4$–5.8, consistent with the expected size evolution of galaxies across this range (e.g., K. Ormerod et al. 2024; A. Genin et al. 2025). We show this in Figure 8. Interestingly, we also find that objects below $z \approx 5$ fall almost entirely in the subsample of LRDs showing complex UV morphology. The number of such LRDs drops significantly from $z \approx 5$ to $z \approx 8$, with only two objects above $z > 7$ still showing clear morphological complexity. This naturally raises the question of whether this is a true effect, where as soon as the Universe matures, these objects start building more extended envelopes or whether this is a selection effect (J.-B. Billand et al. 2025). In the latter case, given the small sample size, we caution that the results may be biased, and a larger sample will be required to robustly confirm these findings.

Although the extended emission revealed in the stacked images is smaller than the $\approx$4–6 kpc hosts identified at $z \approx 2$, it is broadly consistent with the expected size evolution of galaxies. According to A. Genin et al. (2025), disk sizes roughly double between $z \approx 5$ and $z \approx 2$, implying that the compact high-redshift structures we observe could naturally evolve into the more extended hosts seen around systems like the Saguaro at later times. This strengthens the case for a physical connection between canonical LRDs and their potential lower-z analogs.

3.2. The LRD Visibility with Redshift

To further investigate the idea that our view of LRDs at high redshift may be biased, we develop a simple analytic model of surface brightness dimming to quantify how much of an LRD's extended host galaxy becomes undetectable at progressively higher redshifts. We assume the host follows a circular exponential light profile with a central surface brightness I_0 and scale radius R_s

$$I(R) = I_0 \exp\left(-\frac{R}{R_s}\right), \tag{1}$$

where $I(R)$ is the intrinsic surface brightness at galactocentric radius R. The total integrated luminosity of the host is then $L_{\rm host} = 2\pi I_0 R_s^2$.

Due to cosmological surface brightness dimming, the observed surface brightness is reduced by a factor of $(1 + z)^4$ (R. C. Tolman 1930). We define the maximum

[29] However, diagnostic diagrams based on emission lines likely indicate a mixed origin, involving both star formation and AGN activity (P. Rinaldi et al. 2025a).

[30] To do so, we made use of 99 simulated NIRCam PSFs.

[31] All JADES images are already background-subtracted; however, small residuals may still persist. We therefore applied an additional background subtraction after stacking.

[32] The bins were selected to ensure sufficient statistics in each, accounting for the redshift evolution in the number density of LRDs (D. D. Kocevski et al. 2025; V. Kokorev et al. 2024).

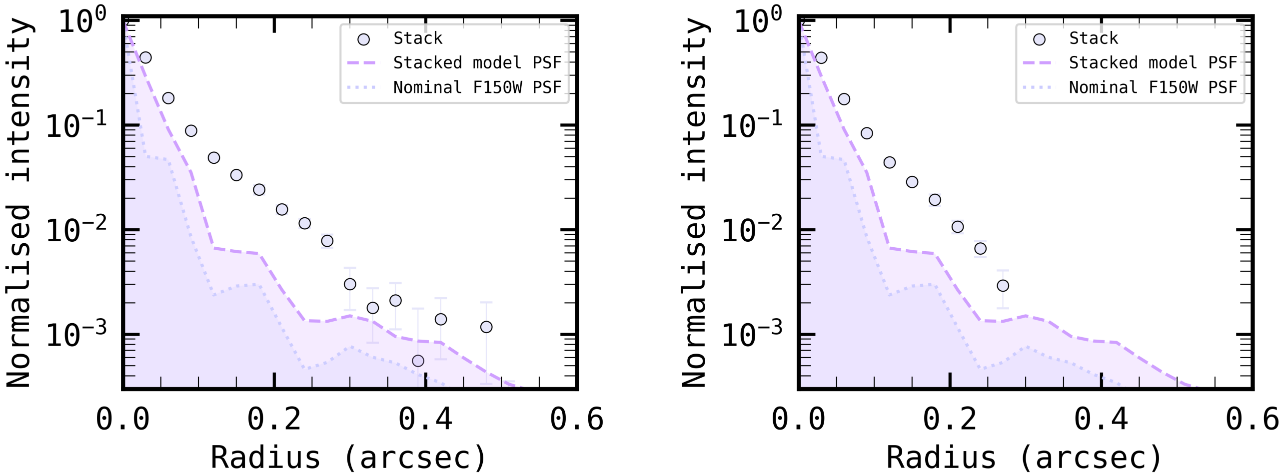

Figure 7. Left: radial profile of the stacked image of 99 photometrically selected LRDs from P. Rinaldi et al. (2025a) in the rest-frame UV (1500–2000 Å). Right: same as on the left, but with the background artificially elevated to the highest level that does not cause the surrounding region to become strongly negative. To emphasize the extended nature of the stacked UV profile of the LRDs, we note that our simulated stacked PSF was constructed using a spatial offset of 1 pixel (≈30 mas for the NIRCam short-wavelength channel), which is significantly larger (≈6×) than the typical internal astrometric scatter in the JADES images, thus representing an upper limit on the observed stacked PSF size. Altogether, this experiment reveals that the radial profile of the stacked LRDs declines less steeply than expected, suggesting that an extended structure may lie hidden beneath the observational noise.

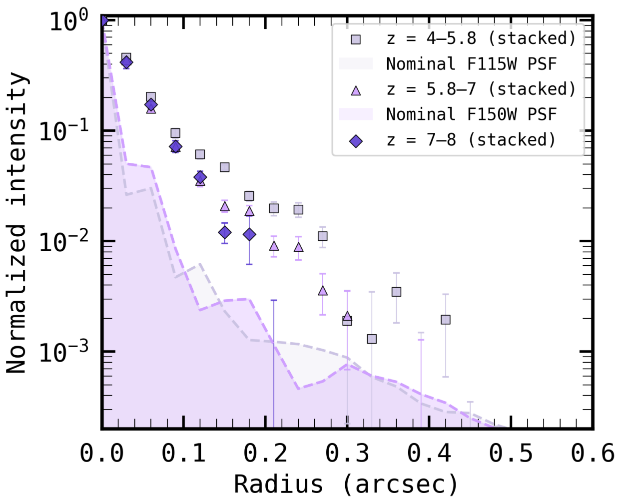

Figure 8. Radial profiles of the stacked rest-frame UV (1500–2000 Å) images of photometrically selected LRDs from P. Rinaldi et al. (2025a), shown in redshift bins. For comparison, the nominal PSFs are overplotted: F115W for $z \approx 4$–5.8 and F150W for $z \approx 5.8$–8. A slight increase in radial extent is observed when moving from the highest to the lowest redshift bin.

detectable radius $R_{\max}$ at which the observed SB equals the detection limit $I_{\lim}$

$$R_{\max}(z) = R_s \ln\left(\frac{I_0}{I_{\lim}(1+z)^4}\right). \tag{2}$$

This expression requires the argument of the logarithm to be larger than 1, which implies $I_0 > I_{\lim}(1+z)^4$. Within $R_{\max}$, the fraction of the total host light that remains detectable is computed as

$$f_{\rm det}(z) = 1 - \left(1 + \frac{R_{\max}(z)}{R_s}\right)\exp\left(-\frac{R_{\max}(z)}{R_s}\right). \tag{3}$$

The fraction lost is then $f_{\rm lost}(z) = 1 - f_{\rm det}(z)$.

To test this simple model, we adopt the following reference values, motivated by observed LRD properties and JWST detection thresholds: $I_0 = 100\,L_\odot\,{\rm pc}^{-2}$ (central surface brightness of the host), $R_s = 1.2$ kpc (scale radius, e.g., $\approx 0\overset{''}{.}2$ at $z = 7$), and $I_{\lim} = 0.0079\,L_\odot\,{\rm pc}^{-2}$ (corresponding to $\mu \approx 28.5$ mag/arcsec^2 in the rest UV). The typical value for I_0 was taken from, e.g., S. Tacchella et al. (2015), for $z = 2$. We compute the lost light fraction for redshifts $z = 2$, 5, 7, and 9. The results are summarized in Table 2. If we also account for the observed redshift evolution of galaxy sizes (e.g., $R_s \propto (1+z)^{-m}$; K. Ormerod et al. 2024; A. Genin et al. 2025), the maximum detectable radius $R_{\max}$ would shrink significantly in physical units, further compounding the loss of extended light at high redshift.

These results show that, even for relatively compact and moderately bright host galaxies, surface brightness dimming can significantly limit the detection of extended components at high redshift. By $z \gtrsim 7$, more than two-thirds of the host light is lost to cosmological dimming, consistent with the observed compact morphologies of LRDs in JWST imaging. This calculation agrees with the model by F. Pacucci & A. Loeb (2025), which proposed that, at $z \gtrsim 8$, the observability of LRDs is significantly suppressed by the cosmological surface brightness dimming. Our results are also consistent with the recent findings of J.-B. Billand et al. (2025).

The surface brightness dimming for high-redshift LRDs is strong enough that we cannot tell if they are truly isolated point-like sources or if they are the nuclei of more extended galaxies.

4. Low-redshift Analogs: How Typical is the Saguaro?

It is not yet clear how to trace LRDs to lower redshifts. For example, a ground-based survey over 3.11 deg^2 by Y. Ma et al. (2026) reports a 1 order of magnitude drop in the LRD number density from $z > 4$ to $1.7 < z < 2.7$, consistent with D. D. Kocevski et al. (2025) and V. Kokorev et al. (2024). In contrast, a wide-area Euclid survey over 63 deg^2 finds

Table 2
Surface Brightness Dimming Effects

z	$R_{\max}$ [kpc]	$f_{\rm det}$	$f_{\rm lost}$
2	5.59	0.914	0.086
5	2.73	0.664	0.336
7	1.35	0.311	0.689
9	0.28	0.024	0.976

numerous LRD candidates at $z < 4$, with number densities increasing down to $z \approx 1.5$–2.5 before declining at lower redshifts (Bisigello (Euclid) et al. 2025). These conflicting results likely reflect fundamental differences in selection methodology.

For instance, Y. Ma et al. (2026) adopt a stringent cut, $(m_{\rm PSF} - m_{\rm CModel}) < 0.016$, highly sensitive to faint, extended halos. Conversely, the Euclid team uses a peak–surface brightness criterion, $\mu_{\max} - m_{\rm pointlike} < -2.6$ mag arcsec^{-2}, which remains sensitive to moderate halos but is somewhat less punitive than the criterion from Y. Ma et al. (2026). The importance of selection criteria is made clear in this section, where we discuss half a dozen proposed low-redshift analogs, all of which appear to have the signature V-shaped SED (or one close to this shape) and are compact, but as summarized in Figure 9 exhibit a wide range of behavior in the longer-wavelength infrared.

As a baseline, X. Lin et al. (2026a) identified three LRD analogs at $z \approx 0.1$ in the SDSS database, across 9376 deg^2. They note the sample is likely incomplete due to SDSS's biases against LRDs. Moreover, their selection criteria also differ from those of both Y. Ma et al. (2026) and Bisigello (Euclid) et al. (2025). Nonetheless, they have demonstrated for the first time that low-redshift analogs *actually exist*!

The examples found by X. Lin et al. (2026a) must be rare, given the very large parent sample (although they recently claimed that their sample is highly incomplete; see discussion in X. Lin et al. 2026b). In fact, canonical LRDs known from existing studies are rare at redshifts less than 4 (e.g., D. D. Kocevski et al. 2025; V. Kokorev et al. 2024; Y. Ma et al. 2026). To understand their evolution we need to identify what they become as they age beyond this point. Of course, it is conceivable that they morph into perfectly ordinary-appearing galaxies (F. M. Khan et al. 2025), in which case following their evolution will be difficult. We take the more optimistic stance that their evolutionary products may retain some LRD-like properties, albeit modified by subsequent evolution and possibly observed during brief or recurrent accretion episodes.

We have argued that LRDs could lie in compact, low-surface-brightness host galaxies at high redshifts. By $z \approx 2$, compared with $z \approx 5$, we can expect the hosts to double in diameter and to have much higher surface densities of star formation (e.g., A. Genin et al. 2025), making the hosts more prominent than for the classical LRDs. We can also expect their interstellar medium (ISM) metallicities to have increased, possibly making their already dust-embedded characteristics even more pronounced.

With these considerations in mind, we list some sibling candidates and show their SEDs in Figure 9, along with both an average SED for canonical LRDs and the SED of the reddest LRD known from P. G. Pérez-González et al. (2024). All of these proposed "siblings" have a flattening of their SEDs short of 1 μm, and some have the signature "V shape." Whether the rest show this shape intrinsically depends on the amount of reddening one needs to correct in the observations. Given the increase in dust expected at the lower redshifts, we do not reject any proposed siblings on the basis of a flat, rather than rising, UV SED.

In addition to the Saguaro (WISEA J123635.56+621424.2), in Figure 9, we show SEDs of the following:

1. The Big Red Dot (BiRD) at $z = 2.33$ (F. Loiacono et al. 2025). It has a unique SED that turns over toward longer wavelengths near 0.5 μm.
2. GN 280754 at $z = 2.26$, advertised as the Rosetta stone of JWST-discovered AGN by I. Juodžbalis et al. (2024).
3. RUBIES-BLAGN-1 at $z = 3.10$. B. Wang et al. (2025a) have modeled the SED of this source in detail, finding that the UV is dominated by hot stars that are moderately obscured, with the turnup in the UV reflecting the result of dereddening.
4. J101326.25+611220.1 at $z = 3.703$ (Y. Toba et al. 2018). In this regard, A. Noboriguchi et al. (2023) called attention to the possible relation of DOGs discovered with Spitzer (e.g., A. Dey et al. 2008) and LRDs, particularly for those DOGs with blue excesses (namely, Blue HotDOGs; e.g., R. J. Assef et al. 2016; A. Noboriguchi et al. 2022). This galaxy is an excellent example.
5. JADES-GS-191056 at $z = 3.139$ (G. Barro et al. 2026a). In the short-wavelength JWST/NIRCam bands, this source is extended with a complex morphology, suggesting a possible interaction or other disturbance to its host galaxy as found for a significant number of LRDs by P. Rinaldi et al. (2025a).
6. WISE J125327.50+254747.6, at $z = 0.485$ (G. Li et al. 2025). The compactness of this source is demonstrated in the imaging of R. C. McGurk et al. (2015). This is a hot DOG, but at an exceptionally low redshift, and with properties suggesting they represent a transient stage of evolution (G. Li et al. 2025).
7. J1025+1402 is one of three sources identified in SDSS by X. Lin et al. (2026a) at $z \approx 0.1$ that closely resemble canonical LRDs. This similarity is evident from the close match between its SED and the average SED of canonical LRDs from P. G. Pérez-González et al. (2024). These sources therefore provide a unique opportunity to study bona fide low-redshift analogs of LRDs and to investigate their physical nature in much greater detail.
8. R. Lin et al. (2025) call attention to some resemblances between LRDs and compact Green Pea AGNs. However the infrared properties of these candidates need to be better constrained before we can classify them with the other LRD siblings.

The following list presents illustrative examples; other LRD siblings likely exist with similar characteristics:

1. There are a number of galaxies related to J123635.56+621424.2 with similar SEDs and point-like HST images, e.g., IRBG2, IRBG4, IRBG5, and IRBG7 in the notation of J. L. Donley et al. (2010; their Table 2). These also have extended host galaxies that would fade in surface brightness and probably not be prominent at the redshifts of classical LRDs.

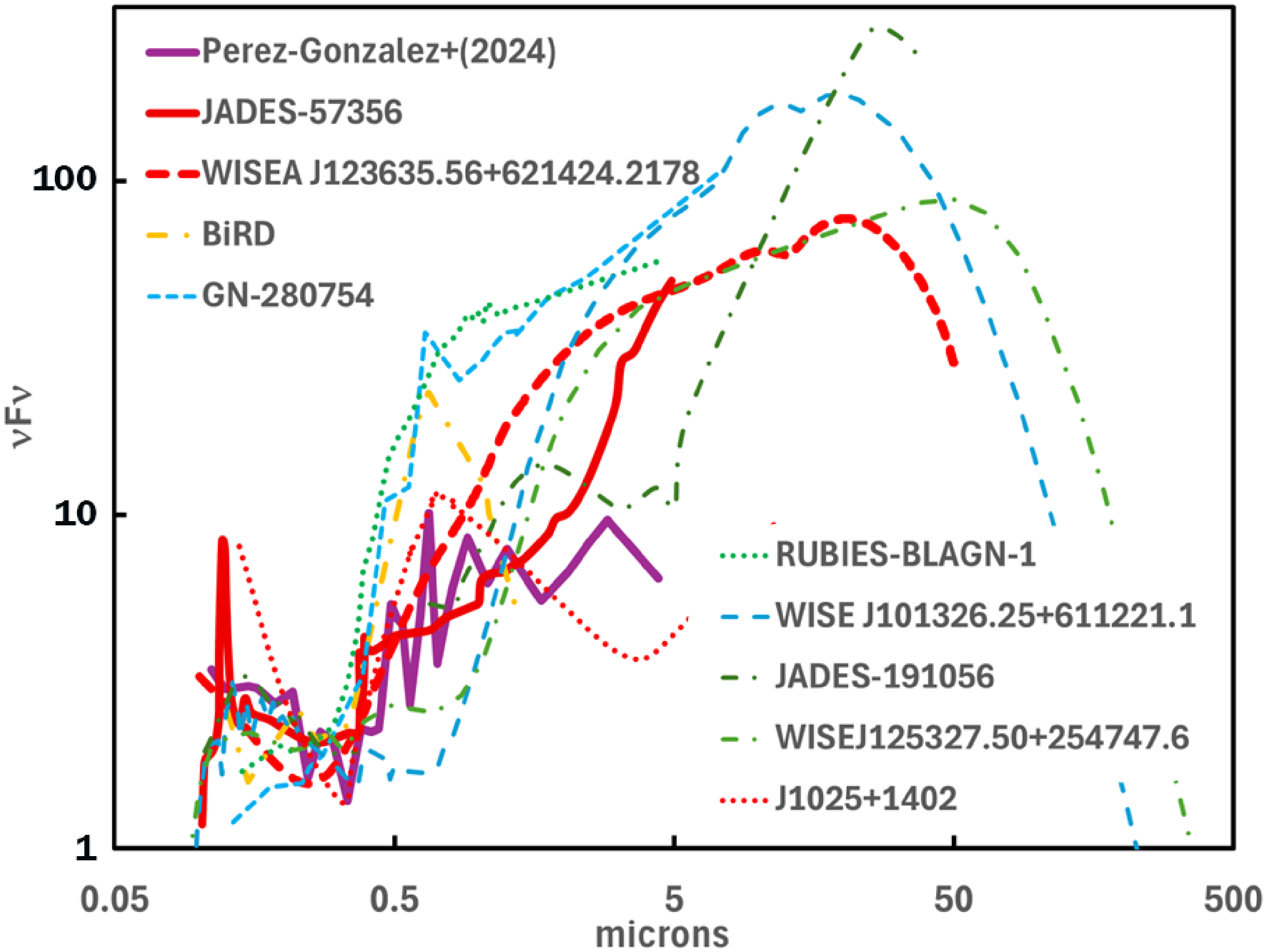

Figure 9. Comparison canonical LRDs with the nuclear SEDs for several relatively low-redshift LRD analogs (at rest-frame wavelengths). The heavy solid lines show (1) the average SED from P. G. Pérez-González et al. (2024); and (2) the reddest example from the same paper, JADES-57356. WISEA J123635.56+621424.2 (i.e., the Saguaro discussed throughout this paper) is the heavy dashed line (the AGN portion only). The others are BiRD from F. Loiacono et al. (2025), GN-280754 I. Juodžbalis et al. (2024); RUBIES-BLAGN-1 from B. Wang et al. (2025c); WISE J101326.25+611221.1, a particularly luminous blue DOG identified by Y. Toba et al. (2018); JADES 191056 G. Barro et al. (2024a); WISE J125327.50+254747 G. Li et al. (2025); and J1025+1402 from X. Lin et al. (2026a).

2. Some Type II quasars have appropriate SEDs (B. Wang et al. 2025b); better high-resolution imaging is needed to confirm that they are sufficiently compact.
3. With two entries already in the list above, it is clear that evaluation among blue DOGs and just DOGs is likely to reveal additional candidates (A. Noboriguchi et al. 2022).

The variety and abundance of these "siblings" is promising, indicating that a more thorough search may reveal additional evolutionary counterparts of classical LRDs at later cosmic time.

5. Discussion and Conclusions

LRDs have become perhaps the most intensively studied high-redshift discovery with JWST. Two of their distinct characteristics are (1) point-like morphology at rest-frame optical wavelengths (e.g., I. Labbé et al. 2023; J. F. W. Baggen et al. 2024; J. Matthee et al. 2024); and (2) high number densities, perhaps a few percent of the population of galaxies at $z > 5$ (D. D. Kocevski et al. 2025; V. Kokorev et al. 2024; P. Rinaldi et al. 2026), but dropping steeply from $z = 4$ to $z = 2$ (Y. Ma et al. 2026). These behaviors raise a fundamental question: if they lack detectable host galaxies, where did they come from, and, as phrased by F. M. Khan et al. (2025), *where have all the LRDs gone?* We address the second question first.

There must be some form(s) of galaxy that includes the descendants of the LRDs. Identifying this evolutionary phase requires understanding which types of galaxies resemble LRDs and tracing them back to the redshifts where LRDs were more prevalent. Since it is unclear what direction their evolution will take, it is important to identify a range of possible descendants. To that end, we have presented a detailed analysis of the characteristics of the Saguaro. Through a detailed AGN–host image decomposition and spatial analysis of its NIRSpec spectrum, we reveal that a "V-shaped" SED arises from its nuclear region. Although the nucleus lies within a face-on spiral galaxy that is clearly visible at $z \approx 2$, we prove, using a toy experiment, that the surrounding galaxy would be virtually undetectable if observed at $z = 7$ due to cosmological surface brightness dimming. This would leave the nucleus entirely "naked," revealing a very compact, heavily dust-embedded AGN with a characteristic "V-shaped" SED, typical of LRDs.

That is, it would readily be identified as a canonical LRD using the limited spectral range provided by the NIRCam filter set at high redshifts. At the moment we are observing it ($z \approx 2$), it is a star-forming ULIRG with a strong submillimeter output. Nonetheless, when this fades (in a few tens of millions of years), it will resemble LRDs even more closely. Thus, it can take its place among the menagerie of objects at redshifts of 2–4 that have been suggested to be related to LRDs.

The disappearance of the host of the Saguaro at high redshifts led us to look in more detail for the potential presence of undetected hosts around canonical LRDs. By stacking the images of the full sample of 99 LRDs from P. Rinaldi et al. (2025a), we found significant excess emission extending to a radius of $0\farcs2$, or ≈2–3 kpc in diameter (when looking at the UV emission). That is, on average canonical LRDs at high redshift tend to lie within an enveloping galaxy that is not apparent at typical imaging depths due to surface brightness dimming. Interestingly, a similar experiment was also performed in the optical by Y. Zhang et al. (2025), who found comparable results, further supporting the presence of faint extended halos in LRDs that likely remain undetected in most NIRCam surveys. An even more compelling case is the recently reported lensed LRD at $z = 3.501$ behind AS1063 ($\mu \approx 2$), identified by V. Kokorev et al. (2026) in the GLIMPSE data (H. Atek et al. 2025), which reach depths of ≈30.5–31 mag at 5σ. This LRD is hosted by a galaxy with $M_\star < 10^{7.5}\,M_\odot$ and $R_{\rm eff} \approx 1$ kpc. Further support comes from the recently identified population of local LRD analogs at $z < 1$ (W. Ding et al. 2026; X. Lin et al. 2026b; K. Park et al. 2026), which also appears, in most cases, to be embedded within extended envelopes, despite the limited spatial resolution of the imaging currently available for these sources.

Finally, we did an analysis of the general expected effects of surface brightness dimming on LRD hosts as a function of redshift. This shows that most of the host galaxy signal slips below typical detection limits by $z = 7$ and hosts are virtually undetectable by $z = 9$. We conclude that current measurements are agnostic as to whether LRDs form in isolation or represent the nuclei of extended host galaxies. This ambiguity likely stems from observational biases: at high redshift, we may be seeing only the bright core, *the tip of the iceberg*, while more extended components either remain undetected due to resolution and sensitivity limits or are still in the process of assembling.

In light of the existence of objects (i.e., LRDs) showing "V-shaped" SEDs from $z \approx 8$–9 down to $z \approx 0.1$, it becomes clear that the "LRD phase" is not exclusive to the early Universe, but may represent a specific evolutionary stage that galaxies undergo under certain (and still unknown) physical conditions. Their compact, red appearance may not indicate a distinct class of objects (as also recently suggested by J.-B. Billand et al. 2026), but rather a transient and observationally biased view of systems that are more extended and complex than they initially appear, with the visible component likely tracing the peak of interaction between the host galaxy and the central (still unknown) engine.

The launch of JWST has undoubtedly transformed our view of the early Universe, greatly enhancing our ability to observe high-z galaxies and fundamentally challenging several aspects of pre-JWST galaxy formation and evolution paradigms. The systematic discovery of LRDs has raised numerous questions about the early growth of black holes and the coevolution of galaxies and SMBHs at high redshift. While uncovering their true nature is fundamental, it is equally important to investigate what these sources may evolve into at later epochs, as this provides crucial insight into galaxy evolution across cosmic time. In this context, the Saguaro may serve as a valuable link, providing a rare test bed in which an LRD-like nucleus can be studied together with its surrounding host galaxy. Future high-resolution spectroscopic follow-up (PID 10311; PIs: P. Rinaldi & E. Iani) will be essential to spatially isolate the compact core, constrain the physical origin of its V-shaped SED, and assess whether, and to what extent, this system is connected to the broader population of high-redshift LRDs.

Acknowledgments

The authors thank the anonymous referee for constructive comments, which helped improve the manuscript. The authors also thank Xiaohui Fan, Xiaojing Lin, Camilla Pacifici, Marianna Annunziatella, Claudia Scarlata, Luis C. Ho, and Pablo G. Pérez-González for valuable discussions.

This work is based on observations made with the NASA/ESA/CSA JWST. The data were obtained from the Mikulski Archive for Space Telescopes (MAST) at the Space Telescope Science Institute, which is operated by the Association of Universities for Research in Astronomy, Inc., under NASA contract NAS 5-03127 for JWST. These observations are associated with JWST programs GTO #1181, GTO #1211, GO #1895, GO #3577, and GO #6434 (F. Sun et al. 2025).

Some of the data products presented herein were retrieved from the Dawn JWST Archive (DJA). DJA is an initiative of the Cosmic Dawn Center (DAWN), which is funded by the Danish National Research Foundation under grant DNRF140.

This research has made use of data obtained from the Chandra Data Archive provided by the Chandra X-ray Center (CXC).

The authors acknowledge the FRESCO team led by PI P. Oesch for developing their observing program with a zero-exclusive-access period. Processing for the JADES NIRCam data release was performed on the lux cluster at the University of California, Santa Cruz, funded by NSF MRI grant AST 1828315. Also based on observations made with the NASA/ESA Hubble Space Telescope obtained from the Space Telescope Science Institute, which is operated by the Association of Universities for Research in Astronomy, Inc., under NASA contract NAS 526555. The data (G. Illingworth 2015; P. Oesch & D. Magee 2023; M. Rieke et al. 2023a; F. Sun & E. Egami 2025) presented in this article were obtained from MAST at the Space Telescope Science Institute.

The authors acknowledge use of the lux supercomputer at UC Santa Cruz, funded by NSF MRI grant AST 1828315.

The work of G.H.R. and P.R. was also supported by grant 80NSSC18K0555, from NASA Goddard Space Flight Center to the University of Arizona.

A.J.B. acknowledges funding from the "FirstGalaxies" Advanced grant from the European Research Council (ERC) under the European Union's Horizon 2020 research and innovation program (grant agreement No. 789056)

B.E.R. acknowledges support from the NIRCam Science Team contract to the University of Arizona, NAS5-02015, and JWST Program 3215.

The research of C.C.W. is supported by NOIRLab, which is managed by the Association of Universities for Research in Astronomy (AURA) under a cooperative agreement with the National Science Foundation.

S.C. acknowledges support by the European Union's HE ERC Starting grant No. 101040227 - WINGS.

Y.Z., Z.J., B.D.J., C.N.A.W., and P.R. gratefully acknowledge the JWST/NIRCam contract to the University of Arizona NAS5-02015.

S.A. acknowledges support from the JWST Mid-Infrared Instrument (MIRI) Science Team Lead, grant 80NSSC18K0555, from NASA Goddard Space Flight Center to the University of Arizona.

R.M., F.D.E. acknowledge support by the Science and Technology Facilities Council (STFC), by the ERC through Advanced grant 695671 "QUENCH," and by the UKRI Frontier Research grant RISEandFALL. R.M. also acknowledges funding from a research professorship from the Royal Society.

L.B. acknowledges financial support from the Inter-University Institute for Data Intensive Astronomy (IDIA), a partnership of the University of Cape Town, the University of Pretoria and the University of the Western Cape, and from the South African Department of Science and Innovation's National Research Foundation under the ISARP RADIO-MAP+ Joint Research Scheme (DSI-NRF grant No. 150551) and the CPRR HIPPO Project (DSI-NRF grant No. SRUG22031677). C.J.E.G. acknowledges the financial assistance of the South African Radio Astronomy Observatory (SARAO) (www.sarao.ac.za).

Facilities: CXO, HST, JWST.

Software: ASTROPY (Astropy Collaboration et al. 2022), BAGPIPES (A. C. Carnall et al. 2019), MSAEXP (G. Brammer 2023)NUMPY (C. R. Harris et al. 2020), PANDAS (T. p. d team 2024)PHOTUTILS (L. Bradley et al. 2016), TOPCAT (M. Taylor 2022), CIAO (A. Fruscione et al. 2006), XSPEC (K. Arnaud et al. 1999), STPSF (M. D. Perrin et al. 2014).

Appendix A AGN–Host Decomposition

We present the results of the AGN–host image decomposition using both HST and JWST/NIRCam data in Table 3. We present the data, model, and residual images in 1.″5 × 1.″5 cutouts in Figure 10. We report the residuals in the ΔFlux metric, which quantifies the percentage difference between the model (AGN + host) and the observed flux within the same aperture. This quantity is evaluated across circular apertures with radii ranging from 0.″1 to 0.″6. Across all HST and JWST bands, the residual flux after AGN–host decomposition remains modest, with average values around 6%–7% and typically below 10% at all apertures, thus leading to a negligible impact on the photometric measurements for both host and AGN. In Figure 11, we show the results of the more sophisticated GALFITM modeling.

We also quantify the relative AGN and host contributions as a function of radius. We find that the central regions are dominated by the point-like component, modeled as an AGN, whereas the host becomes dominant at larger radii (Figure 12).

Table 3
Flux Densities of the AGN and Host Galaxy Across HST and JWST Filters

Band	AGN Flux (μJy)	Host Flux (μJy)
F435W	0.42	0.54
F606W	0.42	0.84
F775W	0.44	1.23
F814W	0.47	1.45
F090W	0.47	2.02
F105W	0.82	2.94
F115W	0.82	4.80
F125W	1.05	5.68
F140W	1.68	7.42
F150W	2.17	9.03
F160W	2.51	8.88
F182M	3.44	13.10
F200W	4.97	15.30
F210M	5.15	16.33
F277W	12.02	23.48
F335M	23.33	30.48
F356W	27.29	33.00
F410M	44.46	37.78
F444W	56.49	41.57

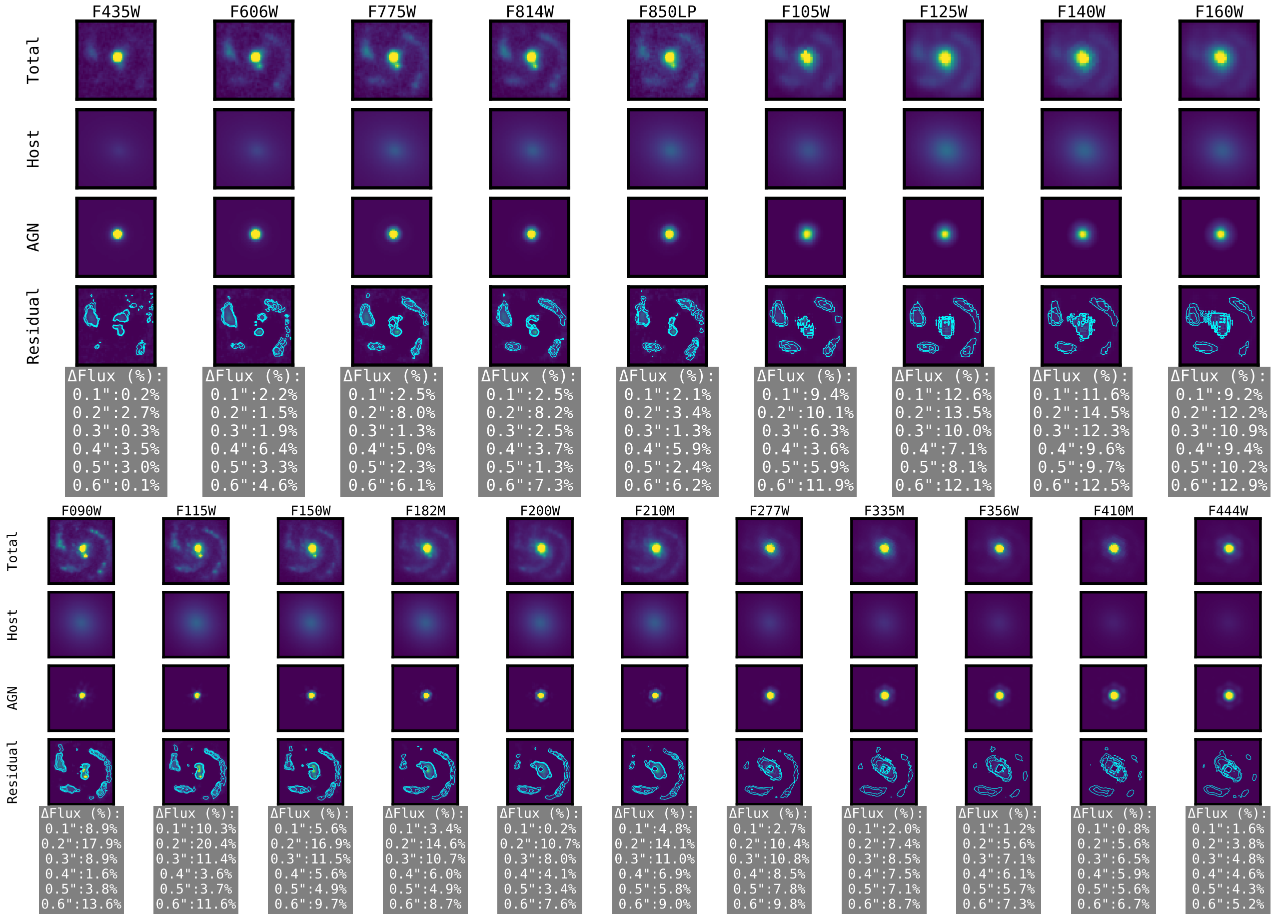

Figure 10. AGN–host image decomposition for HST (top) and NIRCam (bottom). Each cutout is $1\overset{''}{.}5 \times 1\overset{''}{.}5$. The first row shows the original image (total), followed by the host and AGN model components in the second and third rows, respectively. The final row displays the residuals, with overlaid contours highlighting the residual structures. All cutouts are shown using the same scale as the original image in each band.

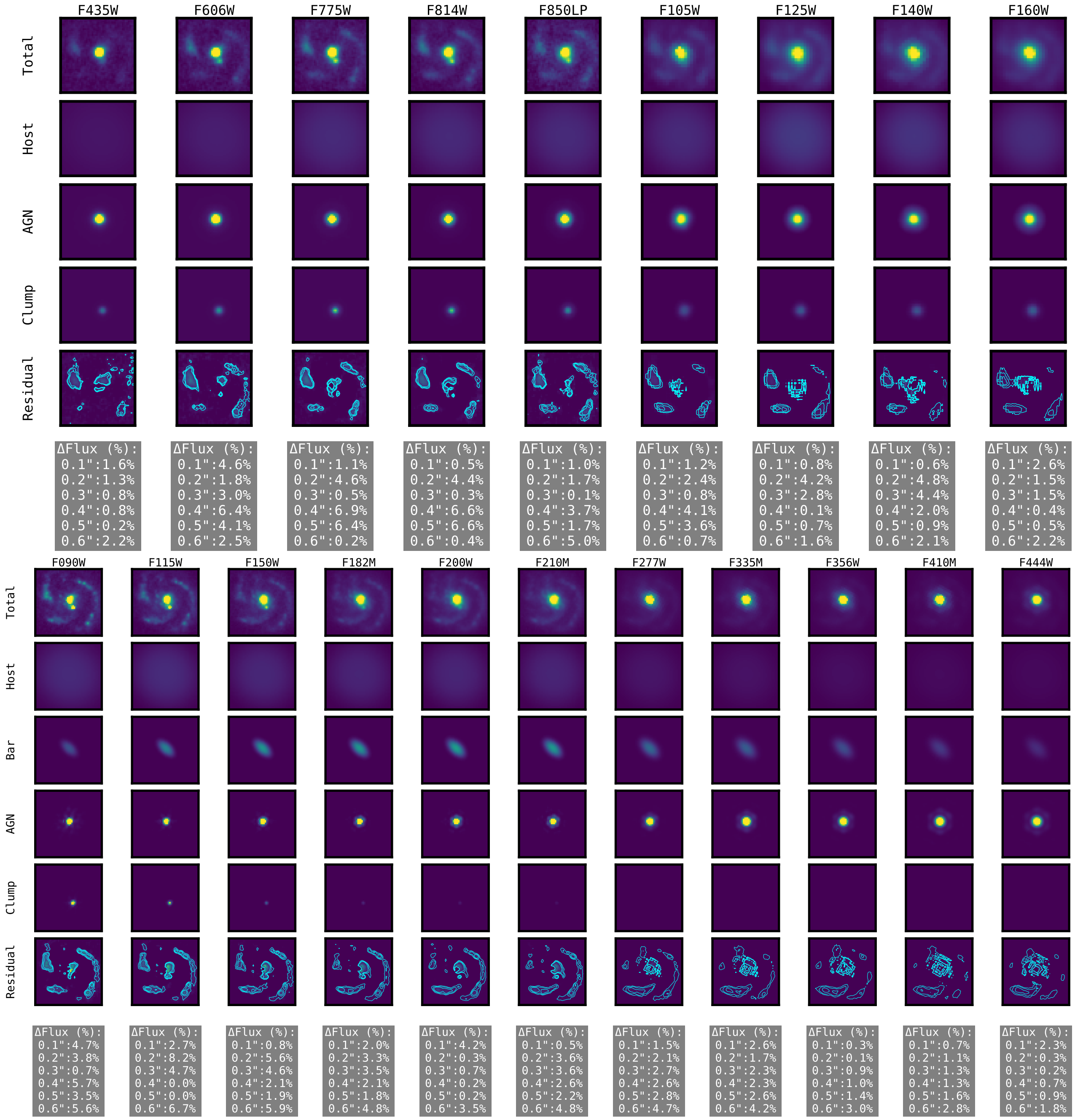

Figure 11. AGN–host image decomposition for HST (top) and NIRCam (bottom) using the more complex models that include additional structural components, namely a clump and, where possible, a bar. Each cutout is 1.″5 × 1.″5. For each band, we show the original image (total), the host model, the AGN model, the additional components included in the fit, and the residuals, with contours highlighting residual structures. Owing to the poorer angular resolution of HST, a bar component cannot be robustly fitted in those filters. Similarly, in the NIRCam long-wavelength channel, the broader PSF prevents a reliable fit of the clump component. Although these more complex models provide improved residuals, the added complexity does not lead to significantly different results compared to our baseline decomposition. All cutouts are shown using the same scale as the original image in each band.

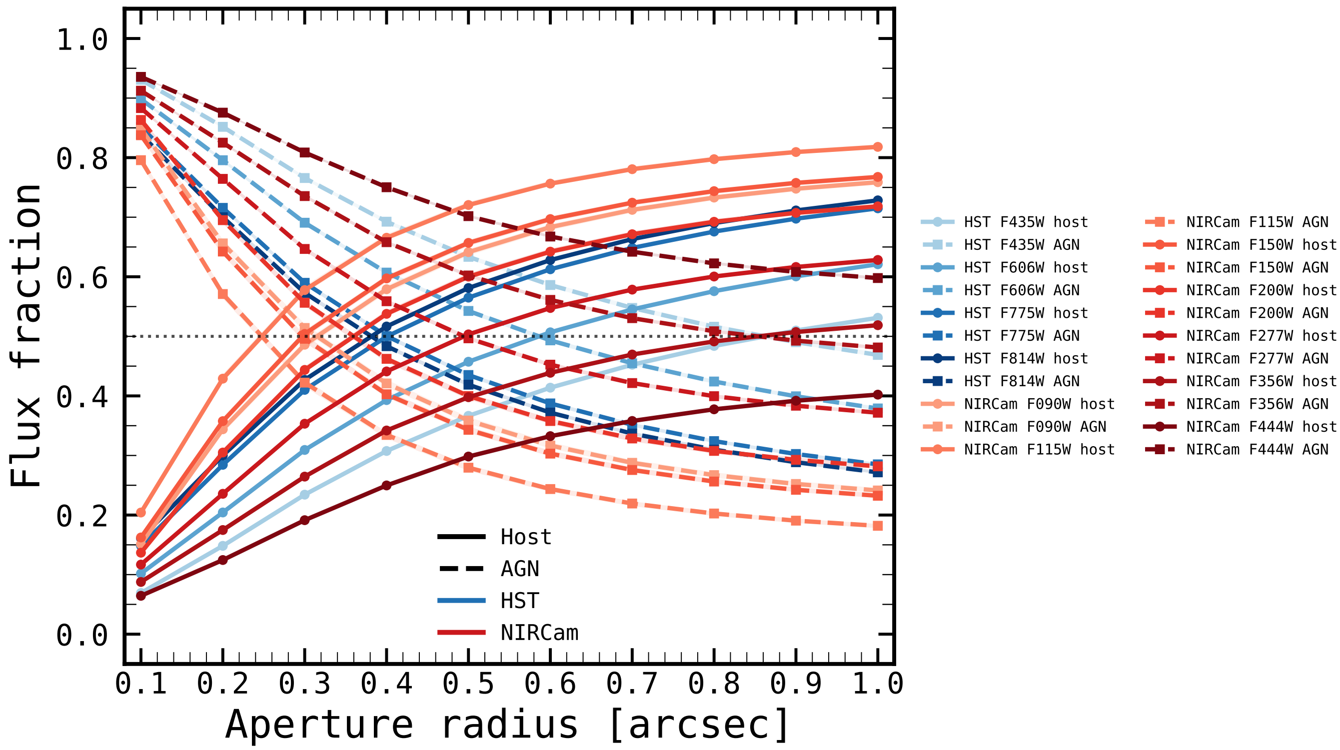

Figure 12. AGN and host fractions as a function of radius, shown up to 1″. The point-like component dominates in the central region, while the host contribution becomes dominant at larger radii.

Appendix B
The Stacked UV Profile of LRDs With Spectroscopic Redshifts

In Figure 13, we show the same panel as in Figure 7, but restricting the analysis to the selected LRDs from P. Rinaldi et al. (2025a) with spectroscopic redshifts and without complex UV morphologies. We note that the statistics are limited in this case, comprising less than one-third of the full sample. Nevertheless, the extended UV stacked profile is still recovered, further supporting the robustness of this result.

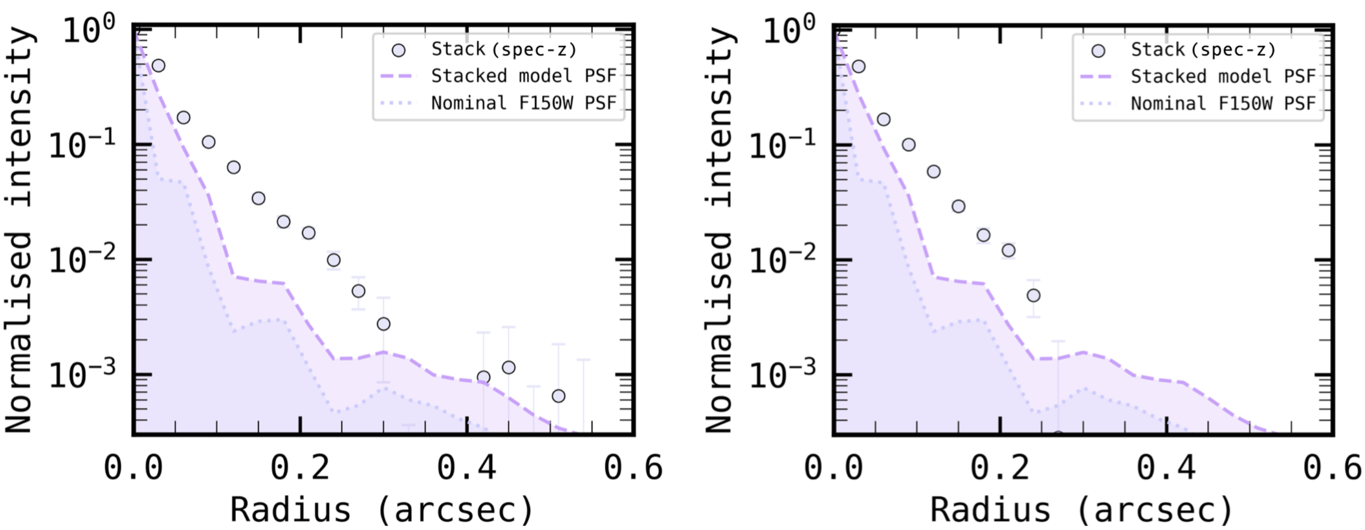

Figure 13. Same as Figure 7, but restricting the stack to LRDs with spectroscopic redshifts and without complex UV morphologies. Despite the smaller sample size, the stacked UV profile remains broader than the simulated stacked PSF, supporting the presence of extended UV emission also in this more conservative subsample.

ORCID iDs

Pierluigi Rinaldi https://orcid.org/0000-0002-5104-8245
George H. Rieke https://orcid.org/0000-0003-2303-6519
Zihao Wu https://orcid.org/0000-0002-8876-5248
Carys J. E. Gilbert https://orcid.org/0009-0001-4012-3043
Fabio Pacucci https://orcid.org/0000-0001-9879-7780
Luigi Barchiesi https://orcid.org/0000-0003-3419-538X
Stacey Alberts https://orcid.org/0000-0002-8909-8782
Stefano Carniani https://orcid.org/0000-0002-6719-380X
Andrew J. Bunker https://orcid.org/0000-0002-8651-9879
Rachana Bhatawdekar https://orcid.org/0000-0003-0883-2226
Francesco D'Eugenio https://orcid.org/0000-0003-2388-8172
Zhiyuan Ji https://orcid.org/0000-0001-7673-2257
Benjamin D. Johnson https://orcid.org/0000-0002-9280-7594
Kevin Hainline https://orcid.org/0000-0003-4565-8239
Vasily Kokorev https://orcid.org/0000-0002-5588-9156
Nimisha Kumari https://orcid.org/0000-0002-5320-2568
Edoardo Iani https://orcid.org/0000-0001-8386-3546
Jianwei Lyu https://orcid.org/0000-0002-6221-1829
Roberto Maiolino https://orcid.org/0000-0002-4985-3819
Eleonora Parlanti https://orcid.org/0000-0002-7392-7814
Brant E. Robertson https://orcid.org/0000-0002-4271-0364
Yang Sun https://orcid.org/0000-0001-6561-9443
Cristian Vignali https://orcid.org/0000-0002-8853-9611
Christina C. Williams https://orcid.org/0000-0003-2919-7495
Christopher N. A. Willmer https://orcid.org/0000-0001-9262-9997
Yongda Zhu https://orcid.org/0000-0003-3307-7525

References

Akins, H. B., Casey, C. M., Lambrides, E., et al. 2025, ApJ, 991, 37
Alexander, D. M., Bauer, F. E., Chapman, S. C., et al. 2005, ApJ, 632, 736
Ananna, T. T., Bogdán, A., Kovács, O. E., Natarajan, P., & Hickox, R. C. 2024, ApJL, 969, L18
Arnaud, K., Dorman, B., & Gordon, C. 1999, XSPEC: An X-ray spectral fitting package, Astrophysics Source Code Library, ascl: 9910.005
Assef, R. J., Walton, D. J., Brightman, M., et al. 2016, ApJ, 819, 111
Astropy Collaboration, Price-Whelan, A. M., Lim, P. L., et al. 2022, ApJ, 935, 167
Atek, H., Chisholm, J., Kokorev, V., et al. 2025, arXiv:2511.07542
Auge, C., Sanders, D., Treister, E., et al. 2023, ApJ, 957, 19
Baggen, J. F. W., van Dokkum, P., Brammer, G., et al. 2024, ApJL, 977, L13
Barchiesi, L., Vignali, C., Pozzi, F., et al. 2024, A&A, 685, A141
Barden, M., Jahnke, K., & Häußler, B. 2008, ApJS, 175, 105
Barro, G., Pérez-González, P. G., Kocevski, D. D., et al. 2024a, ApJ, 963, 128
Barro, G., Perez-Gonzalez, P. G., Kocevski, D. D., et al. 2026a, ApJ, 997, 48
Barro, G., Perez-Gonzalez, P. G., Kocevski, D., et al. 2026b, ApJ, 1003, 96
Bernhard, E., Tadhunter, C., Mullaney, J. R., et al. 2021, MNRAS, 503, 2598
Billand, J.-B., Elbaz, D., Gentile, F., et al. 2025, A&A, 706, A29
Billand, J.-B., Elbaz, D., Franco, M., et al. 2026, arXiv:2604.11677
Bisigello (Euclid), Bisigello, L., Rodighiero, G., et al. 2025, arXiv:2503.15323
Bohn, T., Inami, H., Diaz-Santos, T., et al. 2023, ApJ, 942, L36
Bongiorno, A., Maiolino, R., Brusa, M., et al. 2014, MNRAS, 443, 2077
Borys, C., Smail, I., Chapman, S. C., et al. 2005, ApJ, 635, 853
Bradley, L., Sipocz, B., Robitaille, T., et al. 2016, Photutils: Photometry tools, Astrophysics Source Code Library, ascl: 1609.011
Brammer, G. 2023, msaexp: NIRSpec analyis tools, Zenodo, doi: 10.5281/ZENODO.7299500
Brammer, G. B., van Dokkum, P. G., & Coppi, P. 2008, ApJ, 686, 1503
Brown, M. J. I., Moustakas, J., Smith, J.-D. T., et al. 2014, ApJS, 212, 18
Calvi, V., Stiavelli, M., Bradley, L., Pizzella, A., & Kim, S. 2014, ApJ, 796, 102
Calzetti, D., Armus, L., Bohlin, R. C., et al. 2000, ApJ, 533, 682
Carnall, A. C., McLure, R. J., Dunlop, J. S., et al. 2019, MNRAS, 490, 417
Casey, C. M., Akins, H. B., Finkelstein, S. L., et al. 2025, ApJL, 990, L61
Cash, W. 1979, ApJ, 228, 939
Chen, C.-H., Ho, L. C., Li, R., & Inayoshi, K. 2025, ApJL, 989, L12
Cleri, N. J., Yang, G., Papovich, C., et al. 2023, ApJ, 948, 112
Collaboration, D., Abdul Karim, M., Adame, A. G., et al. 2026, AJ, 171, 285
de Graaff, A., Brammer, G., Weibel, A., et al. 2025c, A&A, 697, A189
de Graaff, A., Hviding, R. E., Naidu, R. P., et al. 2025b, arXiv:2511.21820
de Graaff, A., Rix, H.-W., Naidu, R. P., et al. 2025a, A&A, 701, A168
Del Moro, A., Alexander, D. M., Bauer, F. E., et al. 2016, MNRAS, 456, 2105
Delvecchio, I., Daddi, E., Magnelli, B., et al. 2025, A&A, 704, A313
D'Eugenio, F., Cameron, A. J., Scholtz, J., et al. 2025, ApJS, 277, 4
Dey, A., Soifer, B. T., Desai, V., et al. 2008, ApJ, 677, 943
Dimauro, P., Huertas-Company, M., Daddi, E., et al. 2019, MNRAS, 489, 4135
Ding, W., Kong, X., Guo, W.-J., et al. 2026, A&A, 709, L11
Dojčinović, I., Kovačević-Dojčinović, J., & Popović, L. C. 2023, AdSpR, 71, 1219
Donley, J. L., Rieke, G. H., Alexander, D. M., Egami, E., & Pérez-González, P. G. 2010, ApJ, 719, 1393
Duras, F., Bongiorno, A., Ricci, F., et al. 2020, A&A, 636, A73
Efstathiou, A., Pearson, C., Farrah, D., et al. 2014, MNRAS, 437, L16
Eisenstein, D. J., Johnson, B. D., Robertson, B., et al. 2025, ApJS, 281, 50
Eisenstein, D. J., Willott, C., Alberts, S., et al. 2026, ApJS, 283, 6
Fan, X., Bañados, E., & Simcoe, R. A. 2023, ARA&A, 61, 373
Ferruit, P., Jakobsen, P., Giardino, G., et al. 2022, A&A, 661, A81
Feuillet, L. M., Meléndez, M., Kraemer, S., et al. 2024, ApJ, 968, 91
Fisher, D. B., & Drory, N. 2008, AJ, 136, 773
Fruscione, A., McDowell, J. C., Allen, G. E., et al. 2006, SPIE, 6270, 62701V
Furtak, L. J., Zitrin, A., Plat, A., et al. 2023, ApJ, 952, 142
Förster Schreiber, N. M., Genzel, R., Lutz, D., & Sternberg, A. 2003, ApJ, 599, 193
Gardner, J. P., Mather, J. C., Abbott, R., et al. 2023, PASP, 135, 068001
Gehrz, R. D., Roellig, T. L., Werner, M. W., et al. 2007, RScI, 78, 011302
Genin, A., Shuntov, M., Brammer, G., et al. 2025, A&A, 699, A343
Gilli, R., Norman, C., Vignali, C., et al. 2014, A&A, 562, A67
Gilli, R., Vignali, C., Mignoli, M., et al. 2010, A&A, 519, A92
Gillman, S., Pye, J. P., Alonso-Herrero, A., et al. 2025, A&A, 704, A100
González Delgado, R. M., & Heckman, T. 1999, Ap&SS, 266, 187
Greene, J. E., Labbe, I., Goulding, A. D., et al. 2024, ApJ, 964, 39
Greene, J. E., Seth, A., Kim, M., et al. 2016, ApJ, 826, L32
Hainline, K. N., Maiolino, R., Juodzbalis, I., et al. 2025, ApJ, 979, 138
Hanish, D. J., Capak, P., Teplitz, H. I., et al. 2015, ApJS, 217, 17
Harikane, Y., Zhang, Y., Nakajima, K., et al. 2023, ApJ, 959, 39
Harris, C. R., Millman, K. J., van der Walt, S. J., et al. 2020, Natur, 585, 357
Harrison, F. A., Craig, W. W., Christensen, F. E., et al. 2013, ApJ, 770, 103
Hodge, J. A., Smail, I., Walter, F., et al. 2019, ApJ, 876, 130
Hviding, R. E., de Graaff, A., Liu, H., et al. 2026, ApJ, 1000, L18
Häußler, B., Bamford, S. P., Vika, M., et al. 2013, MNRAS, 430, 330
Illingworth, G. 2015, Hubble Legacy Fields ("HLF"), STScI/MAST, doi:10.17909/T91019
Inayoshi, K., & Maiolino, R. 2025, ApJ, 980, L27
Jakobsen, P., Ferruit, P., Alves de Oliveira, C., et al. 2022, A&A, 661, A80
Ji, X., D'Eugenio, F., Juodžbalis, I., et al. 2026, MNRAS, 545, staf2235
Ji, X., Maiolino, R., Übler, H., et al. 2025, MNRAS, 544, 3900
Juodžbalis, I., Ji, X., Maiolino, R., et al. 2024, MNRAS, 535, 853
Kalita, B. S., Silverman, J. D., Daddi, E., et al. 2024, ApJ, 960, 25
Khan, F. M., Davis, B. L., Macciò, A. V., & Holley-Bockelmann, K. 2025, ApJ, 986, L1
Kido, D., Ioka, K., Hotokezaka, K., Inayoshi, K., & Irwin, C. M. 2025, MNRAS, 544, 3407
Killi, M., Watson, D., Brammer, G., et al. 2024, A&A, 691, A52
Kirkpatrick, A., Pope, A., Sajina, A., et al. 2015, ApJ, 814, 9
Kocevski, D. D., Finkelstein, S. L., Barro, G., et al. 2025, ApJ, 986, 126
Kokorev, V., Caputi, K. I., Greene, J. E., et al. 2024, ApJ, 968, 38
Kokorev, V., Chisholm, J., Naidu, R. P., et al. 2026, ApJ, 1004, 153
Kokorev, V., Fujimoto, S., Labbe, I., et al. 2023, ApJ, 957, L7
Kotilainen, J. K., Reunanen, J., Laine, S., & Ryder, S. D. 2000, A&A, 353, 834
Kriek, M., & Conroy, C. 2013, ApJ, 775, L16
Kroupa, P. 2001, MNRAS, 322, 231
Labbé, I., van Dokkum, P., Nelson, E., et al. 2023, Natur, 616, 266
LaMassa, S., Farrow, I., Urry, C. M., et al. 2025, ApJ, 981, 101
Li, G., Wu, J., Tsai, C.-W., et al. 2025, ApJ, 981, 104
Lin, R., Zheng, Z.-Y., Jiang, C., et al. 2025, ApJL, 980, L34
Lin, X., Fan, X., Cai, Z., et al. 2026a, ApJ, 997, 364
Lin, X., Fan, X., Cai, Z., et al. 2026b, arXiv:2605.21574
Lin, X., Wang, F., Fan, X., et al. 2024, ApJ, 974, 147
Liu, D., Daddi, E., Dickinson, M., et al. 2018, ApJ, 853, 172
Liu, F.-Y., Dai, Y. S., Omont, A., et al. 2024, ApJ, 964, 136
Liu, H., Jiang, Y.-F., Quataert, E., Greene, J. E., & Ma, Y. 2025, ApJ, 994, 113

Loiacono, F., Gilli, R., Mignoli, M., et al. 2025, A&A, 703, A36
Lusso, E., Comastri, A., Vignali, C., et al. 2010, A&A, 512, A34
Lusso, E., & Risaliti, G. 2016, ApJ, 819, 154
Lyu, J., Alberts, S., Rieke, G. H., & Rujopakarn, W. 2022, ApJ, 941, 191
Lyu, J., Alberts, S., Rieke, G. H., et al. 2024, ApJ, 966, 229
Ma, Y., Greene, J. E., Setton, D. J., et al. 2026, ApJ, 1000, 59
Maiolino, R., Risaliti, G., Signorini, M., et al. 2025, MNRAS, 538, 1921
Maiolino, R., Scholtz, J., Curtis-Lake, E., et al. 2024, A&A, 691, A145
Maseda, M. V., de Graaff, A., Franx, M., et al. 2024, A&A, 689, A73
Matthee, J., Naidu, R. P., Brammer, G., et al. 2024, ApJ, 963, 129
Mazzolari, G., Gilli, R., Maiolino, R., et al. 2026, A&A, 706, A372
McGurk, R. C., Max, C. E., Medling, A. M., Shields, G. A., & Comerford, J. M. 2015, ApJ, 811, 14
Murphy, K. D., & Yaqoob, T. 2009, MNRAS, 397, 1549
Naidu, R. P., Oesch, P. A., Reddy, N., et al. 2017, ApJ, 847, 12
Naidu, R. P., Matthee, J., Katz, H., et al. 2025, arXiv:2503.16596
Noboriguchi, A., Inoue, A. K., Nagao, T., Toba, Y., & Misawa, T. 2023, ApJ, 959, L14
Noboriguchi, A., Nagao, T., Toba, Y., et al. 2022, ApJ, 941, 195
Oesch, P., & Magee, D. 2023, The JWST FRESCO Survey, STScI/MAST, doi:10.17909/GDYC-7G80
Oesch, P. A., Bouwens, R. J., Illingworth, G. D., Labbé, I., & Stefanon, M. 2018, ApJ, 855, 105
Oesch, P. A., Brammer, G., Naidu, R. P., et al. 2023, MNRAS, 525, 2864
Oke, J. B., & Gunn, J. E. 1983, ApJ, 266, 713
Ormerod, K., Conselice, C. J., Adams, N. J., et al. 2024, MNRAS, 527, 6110
Pacucci, F., & Loeb, A. 2025, ApJL, 989, L19
Pacucci, F., Nguyen, B., Carniani, S., Maiolino, R., & Fan, X. 2023, ApJ, 957, L3
Padovani, P. 2017, FrASS, 4, 35
Park, K., Torralba, A., Matthee, J., et al. 2026, arXiv:2605.14233
Parlanti, E., Carniani, S., Übler, H., et al. 2024, A&A, 684, A24
Peng, C. Y., Ho, L. C., Impey, C. D., & Rix, H.-W. 2002, AJ, 124, 266
Peng, C. Y., Ho, L. C., Impey, C. D., & Rix, H.-W. 2010, AJ, 139, 2097
Perger, K., Fogasy, J., Frey, S., & Gabányi, K. E. 2025, A&A, 693, L2
Perrin, M. D., Sivaramakrishnan, A., Lajoie, C.-P., et al. 2014, SPIE, 9143, 91433X
Popesso, P., Concas, A., Cresci, G., et al. 2023, MNRAS, 519, 1526
Pérez-González, P. G., Barro, G., Carniani, S., et al. 2026, arXiv:2602.20247
Pérez-González, P. G., Barro, G., Rieke, G. H., et al. 2024, ApJ, 968, 4
Reines, A. E., Greene, J. E., & Geha, M. 2013, ApJ, 775, 116
Rieke, G. H., Alonso-Herrero, A., Weiner, B. J., et al. 2009, ApJ, 692, 556
Rieke, G. H., Buiten, V. A., Goldberg, C. E., et al. 2025, ApJ, 988, 17
Rieke, M., Robertson, B., Tacchella, S., et al. 2023a, Data from the JWST Advanced Deep Extragalactic Survey (JADES), STScI/MAST, doi:10.17909/8TDJ-8N28
Rieke, M. J., Robertson, B., Tacchella, S., et al. 2023b, ApJS, 269, 16
Rinaldi, P., Bonaventura, N., Rieke, G. H., et al. 2025a, ApJ, 992, 71
Rinaldi, P., Hainline, K., D'Eugenio, F., et al. 2026, arXiv:2604.07138
Rinaldi, P., Pérez-González, P. G., Rieke, G. H., et al. 2025b, ApJ, 994, 86
Rujopakarn, W., Rieke, G. H., Weiner, B. J., et al. 2013, ApJ, 767, 73
Rusakov, V., Watson, D., Nikopoulos, G. P., et al. 2026, Natur, 649, 574
Satyapal, S., Vega, D., Heckman, T., O'Halloran, B., & Dudik, R. 2007, ApJL, 663, L9
Setton, D. J., Greene, J. E., de Graaff, A., et al. 2025, ApJ, 995, 118
Severgnini, P., Risaliti, G., Marconi, A., Maiolino, R., & Salvati, M. 2001, A&A, 368, 44
Shen, X., Hopkins, P. F., Faucher-Giguère, C.-A., et al. 2020, MNRAS, 495, 3252
Skelton, R. E., Whitaker, K. E., Momcheva, I. G., et al. 2014, ApJS, 214, 24
Speagle, J. S., Steinhardt, C. L., Capak, P. L., & Silverman, J. D. 2014, ApJS, 214, 15
Stepney, M., Banerji, M., Tang, S., et al. 2024, MNRAS, 533, 2948
Sun, F., & Egami, E. 2025, JWST-GO-03577: Complete NIRCam Grism Redshift Survey (CONGRESS), STScI/MAST, doi:10.17909/6RFK-6S81
Sun, F., Fudamoto, Y., Lin, X., et al. 2025, arXiv:2503.15587
Swinbank, A. M., Smail, I., Chapman, S. C., et al. 2004, ApJ, 617, 64
Tacchella, S., Lang, P., Carollo, C. M., et al. 2015, ApJ, 802, 101
Tang, M., Stark, D. P., Mason, C. A., et al. 2026, arXiv:2604.03563
Taylor, M. 2022, ASPC, 52, 3
T. p. d Team 2024, pandas-dev/pandas: Pandas, Zenodo, doi:10.5281/zenodo.13819579
Teplitz, H. I., Chary, R., Elbaz, D., et al. 2011, AJ, 141, 1
Toba, Y., Ueda, J., Lim, C.-F., et al. 2018, ApJ, 857, 31
Tolman, R. C. 1930, PNAS, 16, 511
Treu, T., & Koopmans, L. V. E. 2004, ApJ, 611, 739
Übler, H., Maiolino, R., Curtis-Lake, E., et al. 2023, A&A, 677, A145
Vulcani, B., Bamford, S. P., Häußler, B., et al. 2014, MNRAS, 441, 1340
Wang, B., de Graaff, A., Davies, R. L., et al. 2025c, ApJ, 984, 121
Wang, B., de Graaff, A., Davies, R. L., et al. 2025a, ApJ, 984, 121
Wang, B., Hennawi, J. F., Cai, Z., et al. 2025b, MNRAS, 539, 1562
Wang, J., & Wei, J. Y. 2010, ApJ, 719, 1157
Whitaker, K. E., Ashas, M., Illingworth, G., et al. 2019, ApJS, 244, 16
Williams, C. C., Alberts, S., Ji, Z., et al. 2024, ApJ, 968, 34
Wirth, G. D., Trump, J. R., Barro, G., et al. 2015, AJ, 150, 153
Xu, J., Sun, M., & Xue, Y. 2020, ApJ, 894, 21
Xue, Y. Q., Luo, B., Brandt, W. N., et al. 2016, ApJS, 224, 15
Yaqoob, T. 2012, MNRAS, 423, 3360
Yue, M., Eilers, A.-C., Ananna, T. T., et al. 2024, ApJL, 974, L26
Zhang, H., Behroozi, P., Volonteri, M., et al. 2024, MNRAS, 529, 2777
Zhang, J., Egami, E., Sun, F., et al. 2026, ApJ, 997, 250
Zhang, Y., Ding, X., Yang, L., et al. 2025, arXiv:2510.25830
Zhong, Y., Chen, X., Ichikawa, K., et al. 2026, ApJL, 1004, L2
Zhuang, M., Li, J., & Shen, Y. 2023, JWST, 3038
Zhuang, M.-Y., & Ho, L. C. 2023, NatAs, 7, 1376